Master's thesis

NTNU
Norwegian University of Science and Technology
Faculty of Engineering
Department of Geoscience and Petroleum

Christoffer Schjem Sørgård

Scalable Infrastructure for Surge and Swab Experiments

Master's thesis in Petroleum Engineering

Supervisor: Sigve Hovda

June 2020

NTNU
Norwegian University of
Science and Technology

Summary

Accurate prediction of downhole pressure variation is of high interest as more complex wells are being drilled within depleted reservoirs and with narrower operational pressure windows. The variation denoted surge and swab is a coupled event where both drillstring dynamics and fluid mechanics have to be taken into account in modeling. An experimental infrastructure has been constructed for benchmarking of such models, as there currently exists few facilities capable of such experiments.

A 66.0 metre vertical three inch well has been constructed with four high accuracy pressure transducers and two temperature sensors along the wellbore. The well was assembled within a ten inch diameter, hundred meter deep pre-drilled well. Contained within the three inch well, sits a 67.8 metre drillstring consisting of half inch drillpipe and a two and half inch BHA connected to a counter weighted axial linear motor. The motor is capable of a stroke length of 1.13 metres, direct implementation of curve motion data and a maximum velocity of 4.9 meters per second with peak force at 2180 Newton. Accurate positional measurements is achieved through a high accuracy one metre tall magnetostrictive sensor rod situated at casing bottom and a position capture sensor within the linear motor. Both motion sensors operating at 1000 Hertz. A complete flow loop is connected to casing top and bottom through a circulation tank and a progressive cavity pump. An air controlled valve is placed at the bottom flow loop entry in order to shut the flow loop during experiments.

The purpose of the experimental infrastructure is to be able to analyze the dynamical pressure variations and drillstring movement associated with surge and swab. The design of the driving force motor allows for a plethora of testing opportunities in terms of string excitation. Specific stroke lengths and reciprocating behaviour as well as rig data can be implemented and tested. The flow loop allows for an uncomplicated exchange of drilling fluid within the well. The installed pump was chosen for its capability of pumping different types drilling fluids utilized in the industry today.

With the size, flexibility of possible experiments and diameter ratio, it is believed to be a field scalable setup. Validation of this can be achieved by implementation of rig data. With drillstring motion data, sample of the drilling fluid in use and similar drillstring ratios, field conditions can be replicated. Under these conditions it will be possible to validate or discard surge and swab models for field use. Though not proven, initial experiments shows great potential for benchmarking models.

The estimated propagation of the excitation through the drillstring was estimated to 11.57 milliseconds. The initial experiments exhibited consistent results with a delay of approximately 30 milliseconds between top and bottom positional measurements during initiation of string excitation. The reason for the additional delay has yet to be accounted for through subsequent experiments. The results are in the same order of magnitude as the expected delay. The additional delay could be due to dampening as well as fluid interaction and that a narrow annular gap is not taken into account. This quantification is beyond the scope of this thesis and should be investigated in future experiments.

Sammendrag

Nøyaktig prediksjon av nedihulls trykk variasjon er av høy interesse da mer komplekse brønner blir boret innenfor depleterte reservoarer og med smalere operasjonelle trykk vindu. Variasjonen betegnet surge og swab er en koblet hendelse hvor både borestrengs dynamikk og fluid mekanikk må tas i betraktning i modellering. En eksperimentell infrastruktur har blitt konstruert for referansemåling av slike modeller, siden det for tiden eksisterer få fasiliteter som er kapable til slike eksperimenter.

En 66.0 meter vertikal tre toms brønn har blitt konstruert med fire høy nøyaktighets trykktransdusere og to temperatur sensorer langs brønnen banen. Brønnen ble montert innenfor en ti tomer i diameter, hundre meter dyp forboret brønn. På innsiden av tre toms brønnen, sitter en 67.8 meter borestreng bestående av halv toms borerør og en to og en halv toms BHA festet til en aksiell lineær motor med motvekt. Motoren er i stand til en slaglengde på 1.13 meter, direkte implementasjon av kurve data og en maksimal hastighet på 4.9 meter per sekund med en kraft på 2180 Newton. Nøyaktig posisjonsmålinger er oppnådd gjennom en høy nøyaktighets en meter høy magnetostriktiv sensor stav plassert på bunnen av brønnen og en posisjonsfangersensor inni lineærmotoren. Begge sensorene opererer ved 1000 Hertz. En komplett strømningssløyfe er tilkoblet til fôringsrøret i topp og bunn gjennom en sirkulasjonstank og en eksenterskruepumpe. Dette gjør det mulig med en ukomplisert sirkulasjon av brønn fluidet. En luft kontrollert ventil er plassert i inngangen til bunnen av strømningssløyfen for å kunne stenge strømningssløyfen under eksperimenter.

Formålet med det eksperimentelle oppsettet er å kunne analysere de dynamiske trykkvariasjonene og borestrengs bevegelser som er tilknyttet surge and swab. Designet av drivkraftmotoren tillater et mangfold av testmuligheter i form av streng eksitasjon. Spesifikke slaglengder og resiprokerende adferd i tillegg til at rig data kan bli implementert og testet. Strømningssløyfen tillater et ukomplisert utbytte av bore fluid i brønnen. Den installerte pumpen ble valgt for sin evne til å pumpe de forskjellige typer bore fluid benyttet i industrien i dag.

Med størrelsen, fleksibiliteten av mulige eksperimenter og diameter forholdet, er det antatt å være et felt skalerbart oppsett. Validering av dette kan bli oppnådd ved implementasjon av rig data. Med borestrengs bevegelse data, prøve av borefluidet i bruk og lignende borestreng forholdstall, feltforhold kan bli gjenskapt. Under disse forholdene vil det være mulig å validere eller forkaste surge og swab modeller for feltbruk. Selv om det ikke er bevist, viser initiale eksperimenter stort potensiale for referansemåling av modeller.

Den estimerte forplantningen av eksitering gjennom borestrengen ble estimert til 11.57 millisekunder. De initiale eksperimentene framviste konsistente resultater med en forsinkelse på 30 millisekunder mellom topp og bunn posisjonsmålinger under igangsetting av streng eksitering. Grunnen for den ekstra forsinkelsen har enda å bli gjort rede for gjennom påfølgende eksperimenter. Resultatet er av samme størrelsesorden som den forventede forsinkelsen. Den ekstra forsinkelsen kan skyldes demping i tillegg til fluid interaksjon og at det smale ringrommet ikke er tatt i betraktning. Denne kvantifiseringen er utenfor omfaget av denne avhandlingen og bør undersøkes i framtidige eksperimenter.

Preface

This thesis was completed at the Department of Geoscience and Petroleum at the Norwegian University of Science and Technology (NTNU) in Trondheim, Norway. The thesis should be considered a continuation of the project report Sørgård (2019) and as the final part of the specialization in petroleum technology in the 5 year MSc program Petroleum Geoscience and Engineering.

I would like to thank my supervisor Sigve Hovda for his excellent assistance in writing this thesis. Additionally i wish to express my deepest gratitude to senior engineers Noralf Vedvik and Steffen Wærnes Moen for their technical support in constructing the experimental setup. Your assistance was essential for the completion of this thesis. Additional acknowledgements are given to Terje Bjerkan and Håkon Myhren for their assistance with technical solutions and manufacturing of parts for the experimental setup.

Furthermore i would like to recognize Bård Torarin Sandahl and Endre Refsnes for your invaluable companionship during my studies. As well as the student organization *Bergstuderendes Forening* for making these five years a treasured experience, Glück Auf.

Finally i would like to thank my family for their endless support during my studies. Without you i would not be where i am today.

Christoffer Sørgård
Trondheim, 30.06.2020

Table of Contents

Summary **1**

Sammendrag **2**

Preface **3**

Table of Contents **6**

List of Tables **7**

List of Figures **12**

1 Introduction **13**

2 HSE and Practicalities **16**
2.1 HSE Consideration 16
2.2 Practical Implications and Covid-19 17

3 Background Theory **18**
3.1 Surge and Swab 18
3.1.1 Models 19
3.2 Added Mass 23
3.3 Basset Forces 23
3.4 Velocity Profile in the Wellbore 24
3.5 Drilling Fluid Rheology 26

4 Experimental Infrastructure **30**
4.1 Casing 30
4.2 Drillstring 33
4.3 Progressive Cavity Pump and Flow Loop 35
4.4 Well and Drillstring Sensors 36
4.4.1 Magnetostrictive Linear Position Sensors 36

4.4.2 Acceleration Sensors 38
4.4.3 Limit Switch 38
4.4.4 Pressure Sensors 38
4.5 Axial linear motor and supporting structure 39
4.6 Communication Driver and Module 42
4.7 Flow Loop 43

5 Design of Experimental Infrastructure 45

6 Preliminary Experiments 47

7 Discussion 51

8 Further Work 53
8.1 Validation 54

9 Conclusion 56

Bibliography 56

Appendix 61

A Supporting Documents 62

B Experimental Infrastructure 68

C Flow Curves from Rheologic Classification 80

D Results from Preliminary Experiments 82

List of Tables

4.1 Pipe specifications of drillpipe, BHA and casing 31
4.2 Specifications of drillstring components 35
4.3 Balluf Magnetostrictive Sensor Specifications 38

List of Figures

3.1 Fluid displacement due to the surge and swab effect where v_p is drillstring speed and v_{ann} is fluid speed with indicated directions. Illustration from Tveit (2016) 18

3.2 Pressure variation and borehole implications of surge and swab due to inertial effects based on downhole measurements from Ramsey (2019) . . 19

3.3 Schematic view of the model of the drillstring. The drillstring is considered as a set of n blocks (m_i) that are connected to n springs with spring constants k_i. Courtesy of Hovda (2018) 22

3.4 Hydrodynamic entrance length and fully developed region with pressure response. Figure from the fluid mechanics textbook White (2010) 24

3.5 Core drag coefficient within the developing region. With diameter ratio, kr, Reynolds number, Rep, and fluid velocity, V_c. From the conference paper Khalil et al. (2008) 26

3.6 Fluid Behaviour and Viscosity models 27

3.7 Viscoelastic fluid and solid response of dynamic oscillatory test. Figures from Anton Paar GmbH: e-learning course – Basics of Rheometry, Anton Paar (2010) 28

3.8 Oscillatory Step Test. 1) Solid state at rest with $G' > G''$. 2) Liquid Behaviour with $G'' > G'$. 3) At rest during structural regeneration with crossover point $G' = G''$ and solid state $G' > G''$. From "Time Dependant Behaviour (Oscillation)" article Anton Paar (2020). 29

4.1 Design proposal for experimental infrastructure from Sørgård (2019) with pressure sensors (P), positional sensors (X) and accelerometers (A). Flow loop equipment of original design proposal contain shear unit, mud hopper and progressive cavity pump. 32

4.2 Illustration of drillstring setup with drillpipe and the bottom 6.0 m BHA. Figure not to scale for illustration purposes. 34

4.3 Wangen KL-30S Progressive Cavity Pump with indicated in- and outflow direction. From "Progressing Cavity Pumps KB-S/KL-S" data sheet, Pumpen (2020) 36
4.4 Magnetostrictive linear position sensor illustration. Figure from paper on differential waveguides, Zhang et al. (2011) 37
4.5 Location of sensors along the well in the experimental infrastructure where X, P and T denotes positional, pressure and temperature sensors respectively. 39
4.6 Linmot linear motor P10-70x320U stator and slider dimensions. Figure from "Linear Motors P10-70x320U" data sheet, LinMot (2020) 40
4.7 Supporting structure for linear motor, counterweight and guide where the motor slider is connected to the drillstring through the slide block attached to the guide. Motor signal cables run to the data acquisition system (DAQ) 41
4.8 Junction box components: 1. DAQ NI USB-6218 data acquisition. Analog input sensor data to digital , 2. 24v power supply , 3. Modbus ethernet/IP gateway , 4. Ground cable for cabinet in case of creeping current from any of the components, 5. LinMot E1400 Servo Drive communication module for linear motor, 6. Cable entry for sensor, motor in feed inlet cables, 7. Distribution of sensory cables , 8. Power fuse of 400 Volt/32 Ampere inlet power, 9. Inlet power main switch 42
4.9 Final design of experimental infrastructure where PT, TT, LT denotes pressure, temperature and positional sensors respectively. V denotes valves and DAQ is the Data Acquisition system with additional cables from the linear motor and pump. Linear motor is attached to the LinMot drive adjacent the DAQ within the junction box. The flow loop is indicated from the mud tank and screw pump to the top and bottom of the casing with the air controlled bottom hole fluid vale V1 on the flow loop controlled by air valve V2 at surface. 44

6.1 Step test 1 positional sensor data from linear motor and bottom hole magnetostrictive sensor rod. Total test time set to 45 seconds. Stroke length set to 100 millimetres. 48
6.2 Step test of experimental infrastructure. A scaled plot of the difference in motor sensor positional data and bottom hole magnetostrictive sensor rod data. Delay equals approximately 30 milliseconds. 49
6.3 Step test 1 raw data from the data acquisition program LabVIEW. Top plot indicating positional sensors. Bottom plot indicating pressure sensor response. Error in labeling, PT1 and PT2 legend is switched. Red line is PT1 and dark blue is PT2. Sensors responding to the movement of the drillstring. Measured surge and swab pressures equal approximately 0.5 bar 50

8.1 Typical deep water blow out preventer (BOP) configuration. Courtesy of Shell International Exploration and Production, 2020 54
8.2 Sample of heave data from the floating drilling vessel Appomattox in the Gulf of Mexico on May 17th. Courtesy of Shell International Exploration and Production, 2020 55

A.1 Lab hours constructing the experimental infrastructure. 62
A.2 Technical data for the LinMot P10-70x320U/1130 motor. 63
A.3 Relationship between the phase current and the position sensor output in the P10-70x320U Motor. SIN+ and SIN- Encoder Signals are Always in Phase With Motor Current Phase U 63
A.4 Technical data for the LinMot E1400 servo drive 64
A.5 Design alteration appraisal submitted by 6th of February and approved by the institute the 12th of February 65
A.6 Standard lower marine riser package HPHT sensor mounted to the BOP stack. Pressure rated from 0 to 20.000 Psi. Courtesy of Shell International Exploration and Production, 2020 66
A.7 Lower marine riser package with HPHT sensor indicated by (45) below Ram 6 at the lower right in the figure. Courtesy of Shell International Exploration and Production, 2020 67

B.1 Safety board instructing required personal protective equipment (PPE) during construction of the experimental infrastructure. From left: Eye protection, Breathing mask, protective footwear, hard hat and hearing protection above. 68
B.2 Casing Mounted in Slips with PVC Sleeve for Temperature Sensor Mount and Steel Spacer below to Avoid Any Damage to the Sensor Fitting 69
B.3 Casing bottom with magnetostrictive, temperature and pressure sensors. Flow loop valve with control tubes 69
B.4 T-joint pressure sensor mount between casing sections. Here during disassembly with water pushed out by the hydrostatic column of remaining water within the casing above the T-joint 70
B.5 Surface slips and casingstring mounted to steel garters at surface 70
B.6 Brass end piece representing the bit and acting as a funnel guide for the magnetostrictive sensor rod at casing bottom 71
B.7 Brass end piece representing the bit and acting as a funnel guide For the magnetostrictive sensor rod at casing bottom schematic. Courtesy of Vedvik, 2020 71
B.8 Rounded crossover between BHA and drillpipe 72
B.9 Rounded crossover between BHA and drillpipe schematic. Courtesy of Vedvik, 2020 72
B.10 Drillstring mounted in surface slips after assembly with sensory cables and flow loop hose running paralell. 73
B.11 Drillstring counterweight and supporting structure before assembly. . . . 73
B.12 Counterweight with plastic guides for sliding within the supporting structure. Counterweight and guide grooved out to account for a weld within the supporting structure. 74
B.13 Mounting of supporting structure for counterweight and motor assembly. Making grooves in the bottom foundation in order to have adjustment possibilities of the structure. Completed in order to properly center the linear motor above the drillstring. 74

B.14 Mounting plate for linear motor on supporting structure. Courtesy of Vedvik, 2020 75
B.15 Chain sprocket at top of supporting structure. Courtesy of Vedvik, 2020 . 75
B.16 Guide rail for guide block to which the linear motor and drillstring is attached. Courtesy of Vedvik, 2020 76
B.17 Supporting structure mounted with guide rail and drillstring attached to slide block 76
B.18 Slide block mounted to guide rail and drillstring with mount for linear motor 77
B.19 Linear motor attached to supporting structure attached to sliding block . . 77
B.20 Honeywell SZL-VL-S-B-N-M Miniature industrial limit switch 78
B.21 Motor and sensory cables attached to the cable canal running into the junction box. 78
B.22 Steel cogwheel with bearings for chain connecting linear motor and counterweight 79

C.1 Anton-Paar MCR 302 Flow curve test with 80 wt-% Glycerol solution. Expressing Newtonian behaviour as it coincides with Newtons law of viscosity ,stated in equation 3.9, with a linear relationship between shear stress,τ, and shear rate,$\dot{\gamma}$. 80
C.2 Anton-Paar MCR 302 Flow curve test with 0.1 wt-% Xanthan gum solution. Expressing non-Newtonian behaviour as it deviates from Newtons law of viscosity ,stated in equation 3.9, with a a non-linear relationship between shear stress,τ, and shear rate,$\dot{\gamma}$. 81

D.1 Step test 2 positional sensor data from linear motor and bottom hole magnetostrictive sensor rod. Data Acquisition malfunction when compiling to file. Last 25 seconds was logged but plot data did not process. Stroke length set to 100 millimetres. 82
D.2 Step test 2 of experimental infrastructure. A scaled plot of the difference in motor sensor positional data and bottom hole magnetostrictive sensor rod data. Delay equals approximately 25 milliseconds. 83
D.3 Step test 2 raw data from the data acquisition program LabVIEW. Top plot indicating positional sensors. Bottom plot indicating pressure sensor response. Error in labeling, PT1 and PT2 legend is switched. Red line is PT1 and dark blue is PT2. Sensors responding to the movement of the drillstring. Measured surge and swab pressures equal approximately 0.5 bar. 84
D.4 Step test 3 positional sensor data from linear motor and bottom hole magnetostrictive sensor rod. Stroke length set to 100 millimeters. Total test time set to 45 seconds. 85
D.5 Step test 3 of experimental infrastructure. A scaled plot of the difference in motor sensor positional data and bottom hole magnetostrictive sensor rod data. Delay equals approximately 30 milliseconds. 85

D.6 Step test 3 raw data from the data acquisition program LabVIEW. Top plot indicating positional sensors. Bottom plot indicating pressure sensor response. Error in labeling, PT1 and PT2 legend is switched. Red line is PT1 and dark blue is PT2. Sensors responding to the movement of the drillstring. Measured surge and swab pressures equal approximately 0.5 bar. 86

Chapter 1

Introduction

Accurate determination of downhole pressure is critical in order to stay within the operational pressure window i.e between the pore and fracture pressure gradient. Failure to do so may cause formation fracture, lost circulation and well control issues. Fracturing of the formation may lead to loss of drilling fluid to the formation which will lower the amount of fluid in the well. This will in turn lower the hydrostatic pressure in the well that may lead to influx from the formation which can result in a kick and in the worst case, a blowout. A drilling fluid with insufficient density will result in the same situation.

A key area of interest in the industry today is the induced pressure variations due to drillstring and casing movement denoted surge and swab where surge is a pressure increase and swab is pressure decrease due to string movement. These pressure variations are encountered during tripping operations and heave motion from floating drilling vessels. The latter is of specific interest as the string follows the motion of the rig when the string is set in the slips on the drillfloor. In this situation, the active and passive heave compensation of the topdrive is not engaged. Though there exists heave compensated drillfloors, it is not common in the industry. The effective pressure surge is strongly related to the tripping speed of the drillstring, fluid rheology, wellbore geometry, flow regime and whether the pipe is open for flow or closed (Crespo et al. (2012). Surge and swab is a coupled problem where drillstring dynamics and fluid mechanics have to be considered and quantified in order to truly explain the nature of induced pressure variations. The challenge of predicting surge and swab can be approached in several ways. The pressure variation can be investigated using drillstring or hydraulics models by means of computer simulations, through field data or from experimental endeavours. Various approaches has been utilized in order to accurately depict the effects of surge and swab. In Fontenot and Clark (1974) a hydraulics model using flow equations was made for determining surge and swab pressures. In Hovda (2018) a model was established with focus on a lumped element method for quantifying the drillstring dynamics as well as integrating elements of fluids mechanics of flow.

Several experimental approaches have been made in order to determine and optimize challenges encountered during drilling operations. The Ullrigg full size offshore-style triple rig by NORCE in Stavanger, Norway. With its seven full scale wells has the capability of testing multiple drilling parameters. With this setup it is possible to do full scale experiments, but since the wells are full scale they do not have sufficient sensory equipment for accurate determination of the down hole drillstring movement and pressure variation associated with surge and swab.

Other institutions have made important experimental setups for accurate determination of different challenges encountered in drilling operations. The TU Clausthal Drilling Simulator Celle in Celle, Germany. With its VR software simulator and pressurized 23 m horizontal experimental drilling rig for investigation of HPHT horizontal drilling. Sintef Petroleum Research experimental flow loop setup in Trondheim, Norway. Consists of a variable inclination test section with the possibility of sand injection and free whirling rotational inner string to investigate cuttings transport and mechanical friction of cuttings. The Texas A&M Multiphase Flow Loop Tower Lab in College Station, Texas. A 140 ft tall vertical flow loop structure with up to 6" inner diameter pipe to investigate two phase flow upwards. Though important for their area of investigation, none of these are set up for surge and swab quantification.

The experimental infrastructure constructed in conjunction with this thesis, consists of an axially reciprocated drillstring within a fluid filled well. The experimental infrastructure is fitted with high accuracy pressure transducers and temperature sensors along the wellbore in order to quantify the effects of surge and swab that is imparted on the fluid from the drillstring. High accuracy positional sensors allows for accurate monitoring of the drillstring movement at the top and bottom of the well. After extensive literature review it is evident that there are currently no experimental setups comparable to the scale and accuracy of the experimental infrastructure constructed in conjunction with this thesis. With the specific focus on surge and swab pressures due to string movement, the setup is the only one of its kind.

The original scope of this thesis was to study the effect drilling fluids with rheologic properties have on the induced surge and swab pressures. The outbreak of the global Covid-19 pandemic caused severe delays to the thesis as a whole. The focus was then redirected towards the functionality and accurate design of the experimental infrastructure. This allowed for a efficient construction of the setup when this became possible. The setup was completed in due time for initial testing.

A limited amount of tests were conducted. These tests were carried out in order to test the functionality of the experimental infrastructure. Three step tests with equal stroke length and speed was conducted and the results exhibit a top to bottom delay of 30 milliseconds. A delay of 11.57 milliseconds was expected for the travel time through stainless steel in air. The reason for the full delay has yet to be accounted for through subsequent experiments. The fluid and string compressibility has not been taken into account, nor the narrow annular gap between the casing and BHA. The functionality of the setup was confirmed with accurate pressure and positional sensor readings as well as a continuous axial movement during experiments confirming mechanical functionality.

In this thesis a literature study on surge and swab and a model review is presented followed by a study on the impact of drilling fluid rheology. A detailed presentation of the experimental infrastructure and its components followed by a discussion on its design from a practical and scientific relevance standpoint. Initial testing of the experimental infrastructure and results from this is presented followed by a discussion on the thesis as a whole. Lastly a suggestion on further work with the experimental infrastructure before a conclusion.

Chapter 2

HSE and Practicalities

2.1 HSE Consideration

The experimental infrastructure is situated in the lab of the Hall building adjacent the Petroleum Teknisk Senter (PTS) facility in Trondheim, Norway. The structure is built in conjunction with a four story fixed scaffolding within the lab. This lab contains several experimental setups and is utilized by NTNU staff and students as well as SINTEF staff. As an HSE measure there is a mandatory safety briefing that has to be completed in order to be granted access to the lab. This demonstration entail the code of conduct consisting of the safety minded behaviour desired when in the lab, fire regulations and required personal protective equipment (PPE). When entering the work-zone of the lab there is a mandatory requirement of safety goggles at all times. Whenever extra safety precautions in regards of PPE, the safety board is to be updated with the added risk factor and required PPE. The safety board is seen in figure B.1 in appendix. With this in mind, HSE considerations was of great importance as there are active experiments and people within the lab at different times. Some of the major considerations during construction of the experimental infrastructure was work conducted at height in each floor of the scaffolding, the gantry crane was actively in use and heat work with the use of grinders and welding machines. When this type of work was in session, the safetyboard was updated with the additional risk and PPE requirements being hard hat, flame resistant clothing, shock resistant footwear and ear protection.

The work was conducted in a safe manner with no unwanted incidents during construction. This was achieved by utilizing a safety minded approach to every part of the construction process. At all times during heat work, fire extinguishers and a fire hose was in the immediate vicinity and flammable objects were removed. During lifting operations, all non-critical personnel was vacated from the area while the operating personnel wore proper PPE and took the necessary precautions regarding falling objects. When the experimental infrastructure was completed new risks regarding experiments arose where pinching points is the major one. As the drillstring is set in motion, all personnel had to stand back with no contact with the rig during experiments.

2.2 Practical Implications and Covid-19

The initial project Sørgård (2019) resulted in a design proposal of a new experimental infrastructure. In collaboration with senior engineers at NTNU, the full order of parts and equipment was made by the end of January. The price estimate in figure A.5 was submitted and the institute were willing to invest in the project with funding confirmed in the middle of February. The total order had different parts from different manufacturers which led to a wide range of estimated deliveries. As further work conducted by engineers at NTNU continued, additional parts were ordered which prolonged the estimated arrival of parts. A potential partnership with an oil service company introduced some design requirements which had to be determined. This communication was a prolonged process that lead to the final ordering of parts to be further delayed.

On the 12th of March 2020 the Norwegian government introduced the strongest and most intervening measures during peace time in Norway due to the global Covid-19 virus outbreak (Regjeringen (2020)). On the same day, NTNU cancelled all lectures and activity on campus and NTNU facilities. With this shutdown, NTNU stopped all outgoing orders and shipments to the its facilities. The Covid-19 shutdown of the NTNU facility lasted until the 27th of April where NTNU opened for critical staff and students completing their final thesis to return to their facilities. But even with the reopening of the lab facilities, the necessary parts and equipment for the experimental infrastructure was still in shipment or delayed.

The focus of the thesis was at this point shifted from experiments with drilling fluids containing rheologic parameters, to properly designing and engineering the scaled experimental infrastructure. With this planning and preparation it was possible to continuously construct the experimental infrastructure when construction commenced.

When work at the lab facility was allowed, additional projects with other students was prioritized as the total work load was less and those projects were able to be completed in a shorter time frame. On the 6th of May it was possible to dismantle the existing experimental setup. Construction of the new experimental infrastructure was able to commence June 3rd with completion of the fixed structure on June 16th. Additional wiring and programming was necessary to test the setup. Due to the amount of work necessary to complete project, i assisted the senior engineers in the construction and engineering phase of the project as seen in figure A.1. After a great collaboration with senior engineers and mechanics at NTNU, we were able to complete construction of the experimental infrastructure in due time for initial testing to be conducted the 26th of June.

Chapter 3

Background Theory

3.1 Surge and Swab

Pressure control is one of the most important factors during drilling and well intervention operations. The main barrier against formation pressure is the hydrostatic pressure created by the drilling fluid within the well. Any pressure fluctuation is therefore critical to predict and control. The surge and swab effect is the term of pressure fluctuations due to drillstring movement known as tripping in and out of the well. When the drillstring is tripped into the well, the string acts as a piston which creates a pressure increase in the well known as the surge effect. Tripping out creates a pressure reduction in the well known as the Swab effect. The friction force acting on the string is defined as the hydrodynamic viscous drag which is the resistance to pipe movement (Ramsey (2019)). This is illustrated in figure 3.1 where the drag is seen closer to the drillstring.

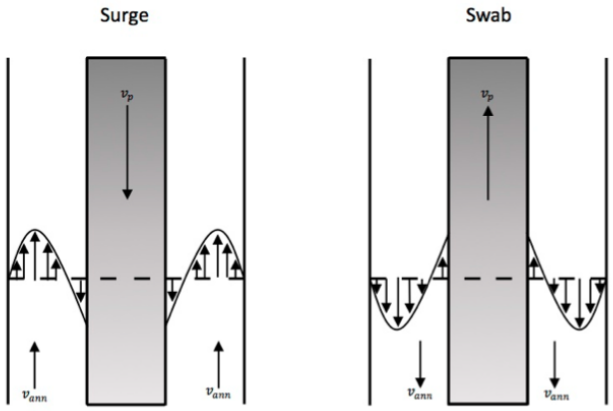

Figure 3.1: Fluid displacement due to the surge and swab effect where v_p is drillstring speed and v_{ann} is fluid speed with indicated directions. Illustration from Tveit (2016)

The implications of uncontrolled pressure variations can be severe to well control. It may lead to fracturing of the formation, loss of drilling fluid to the formation, susceptible to influx in the well, wall cavings, kick and in the worst case, a blowout (IADC (2015). During a stationary situation where the drillstring is hung off in the slips on a floating drilling vessel, the string will follow the heave movement of the rig. When the string is in the slips on the drill floor there is no active or semi-active heave compensation of the string like there is in the top drive and drawworks Huang et al. (2008). As the drillstring is following the movement of the vessel, it can create pressure fluctuations. This may in turn cause hole sloughing or unstable hole conditions which may result in cavings from the borehole wall Moore (1974). If the heave motions of the rig excite any of the resonant frequencies in the drillstring, the motion downhole can be severely amplified because the motion can be substantially underdamped Hovda (2018). This may in turn create large surge and swab pressures or damage the string and tools downhole. The parameters which surge and swab depend on are in general the drillstring tripping speed, wellbore geometry, flow regime, fluid rheology and whether the pipe is hollow or not (Crespo et al. (2012). The pressure variations due to surge and swab as well as the implications of such variations are illustrated in figure 3.2.

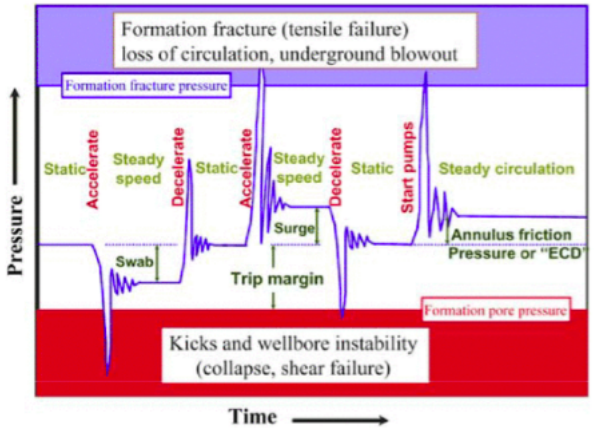

Figure 3.2: Pressure variation and borehole implications of surge and swab due to inertial effects based on downhole measurements from Ramsey (2019)

3.1.1 Models

In order to quantify the pressure variation in a well due to surge and swab, the fluid mechanics as well as the dynamics of the drillstring itself has to be taken into account. Different approaches exists in order to quantify the effect of surge and swab. Quantification based on extensive hydraulics models have been made in Fontenot and Clark (1974) using flow equations for different viscosity models, Crespo and Ahmed (2012) using a narrow-slot hydraulic approach and further work in Crespo et al. (2012) with a numerical approach considering fluid and wellbore compressibility as well as pipe elasticity. Here the effects of compressibility and elasticity are neglected in the beginning to start the iterative cal-

culation. In Gjerstad et al. (2013) a model predicting pressure variation in real time for Heschel-Bulkley fluids based on differential pressure equations was established.

Several drillstring models exists with various physical approximations. In the papers by Tucker and Wang (1999, 2000) a Cosserat model is applied considering the rotational and lateral motions while drilling in a vertical well with focus on the vibrational states. In Arvani et al. (2015) the coupled axial and rotational motion of the drillstring of a floating vessel is modeled using a bond graph model. The model focuses on the effect of heave motion during drilling. A downhole pressure model which takes temporal effects into account with the assumptions of Newtonian fluid and a rigid drillstring is made in Landet et al. (2013). The model focuses on heave-induced pressure fluctuations within the first natural frequency of the drillstring to accommodate the rigid drillstring model. A model using a Stribeck friction model to obtain a nonlinear damping model was studied in Zhao et al. (2016) where the effect of heave motion on a non-rotating drillstring in a curved borehole was studied. This was to simulate the heave induced movement while the drillstring is hung off in the slips on the drillfloor during a drilling operation. These heave motions may induce strong pressure variations by axial stick-slip of the drillstring which have strong nonlinear effects.

A different approach for quantifying the pressure response from surge and swab was conducted in Hovda (2018). A semi-analytical model was constructed which has the benefit of better interpretation. The method has the potential of being combined with real time measurements and used to benchmark more complex models. This was accomplished by creating a lumped element model where damping is due to skin friction from time dependent Newtonian annular Couette-Poiseuille flow. The model is restricted to Newtonian fluids and concentric uniaxial movement in a vertical well. The fluid mechanics is simplified by making certain assumptions focusing on the most influential fluid effects. The drillstring is modelled as a set of n blocks connected sequentially by n spring elements as seen in figure 3.3. The blocks are modelled with zero length and a distance between them, $h = L/n$. The cross-sectional area of the blocks are different which allows for the different dimensions of the bottom hole assembly (BHA) to be accounted for.

The coordinate of each block is denoted by $Q_i(t)$, where t is time. In a case where all springs are not in compression and not in tension, the coordinate of $Q_i(t)$ is ih. $q_i(t)$ is defined by $Q_i(t) = ih + q_i(t)$. The physical state of the drillstring at any time is then uniquely defined by the generalized coordinates $q_i(t)$ and $Q(t)$.

Newton's second law on each block element is then given by

$$\begin{aligned} -m_1\ddot{q}_1 + m_1 g BF_1 - k_1(q_1 - Q) + k_2(q_2 - q_1) + R_1 &= 0 \\ -m_i\ddot{q}_i + m_i g BF_i - k_i(q_i - q_{i-1}) + k_{i+1}(q_{i+1} - q_i) + R_i &= 0 \quad \text{for } 2 \leq i \leq n-1 \\ -m_n\ddot{q}_n + m_n g BF_n - k_n(q_n - q_{n-1}) + R_n &= 0, \end{aligned} \tag{3.1}$$

where m_i is the mass of block i and k_i is the spring constant of the spring above block i. g is the gravity constant and BF_i is the buoyancy factor. Where all the BF_i are all equal to one except elements where the pipe diameter is changing, where the first and last

element of the BHA are examples of this. With the exception of the buoyancy forces, all forces from the drilling fluid are denoted R_i.

When accounting for the forces from the drilling fluid within the well, the assumptions of Newtonian fluid, laminar flow, axial symmetric and all radial and swirl components are equal to zero are made. Under these assumptions the Navier-Stoke momentum equation in three-dimensional cylindrical coordinates can be applied to determine the forces from the drilling fluid. From the assumptions it becomes clear that the pressure p_i in the annulus of the well is a function of the axial coordinate alone and the third momentum equation is reduced to

$$\frac{1}{r}\frac{\partial}{\partial r}\left(r\frac{\partial u_i}{\partial r}\right) = \frac{1}{\mu}\left(\frac{\partial p_i}{\partial z} - \rho_m g\right) + \frac{\rho_m}{\mu}\frac{\partial u_i}{\partial t}. \tag{3.2}$$

Where μ is the viscosity, ρ_m is the mud density and u_i is the axial velocity component of a fluid particle, with distance r from the center of the hole. The assumption that the viscous damping force is a sum of the steady-state force and a Basset force is made. As well as the effect of virtual mass is taken into account. Through further derivation of the well fluid velocity in Hovda (2018), in the case of annular flow with no-slip condition on the inner pipe section, the pressure P_i in the annulus is expressed as

$$P_i = h\sum_{j=1}^{i}\frac{\partial p_j}{\partial z} = \rho_m g h i + \frac{4\mu V h}{\pi R^4}\sum_{j=1}^{i}\psi_j + \frac{4\mu h}{R^2}\sum_{j=1}^{i}\phi_j\dot{q}_j. \tag{3.3}$$

Here the first term is the hydrostatic pressure, the second term is proportional to velocity V and is a dynamic friction term. The third term is also a dynamic friction term that is only related to the movement of the drillstring.

Through further derivation in Hovda (2018) the Basset forces $R_{i,ba}$ on the drillstring is approximated by

$$R_{i,ba} = 2Rh\sqrt{\pi\rho_m\mu}\left(\frac{\alpha_i}{1-\alpha_i^2}\right)\left(t^{-\frac{1}{2}} *_t \ddot{q}_i\right) = b_i(t^{-\frac{1}{2}} *_t \ddot{q}_i). \tag{3.4}$$

And the added mass effect is approximated by

$$\ddot{q}_n\rho_m\pi\alpha_1^2R^2L\frac{1}{n}\sum_{j=1}^{i}\frac{\alpha_j^2}{1-\alpha_j^2}. \tag{3.5}$$

On this basis, an equation for the pressure fluctuation at various parts in the annulus for any topside movement is approximated by

$$\begin{aligned}\Delta P_j(\tau) =& \frac{4\mu c_s}{R^2 n}\sum_{k=1}^{j}\phi_k(\alpha_k)\dot{y}_k + \sqrt{\frac{\rho_m\mu}{\pi}}\frac{2c_s^{\frac{3}{2}}}{L^{\frac{1}{2}}R(1-\alpha_j^2)n}\sum_{k=1}^{j}\left(\frac{\alpha_k}{1-\alpha_k}\right)\left(\tau^{-\frac{1}{2}} *_\tau \ddot{y}_k\right)\\ &+ \left(\frac{\rho_m c_s^2}{Ln}\sum_{k=1}^{j}\frac{\alpha_k^2}{1-\alpha_k^2}\right)\ddot{y}_j.\end{aligned} \tag{3.6}$$

The first term is related to the steady state viscous forces and the third term is the virtual mass term. The second term is the addition related to the Basset forces on both the drillstring and the wellbore wall.

The semi-analytical model showed that the effect of added mass and Basset forces had a significant effect on the downhole pressure and range of the resonant frequencies.

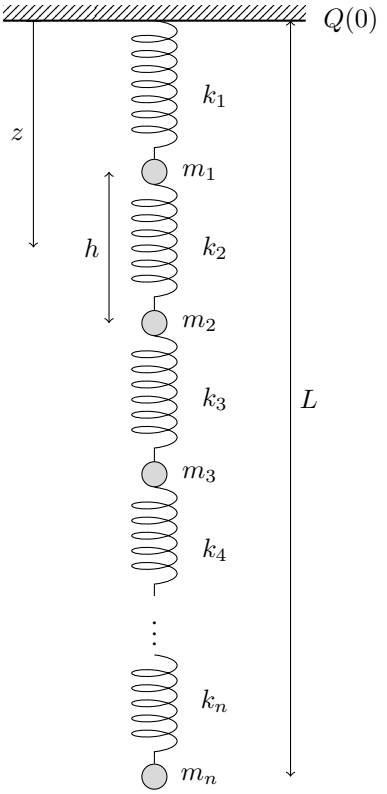

Figure 3.3: Schematic view of the model of the drillstring. The drillstring is considered as a set of n blocks (m_i) that are connected to n springs with spring constants k_i. Courtesy of Hovda (2018)

3.2 Added Mass

As outlined in Sørgård (2019) The added mass effect is a term accounting for the force from the fluid acting on an object during unsteady motion of bodies under water or unsteady flow around objects. According to Sarpkaya (2010), what is imparted to the fluid (or the body) is positive or negative accelerations or inertia (per unit mass) or changes in kinetic energy that are due to the motion of the body, which can be negative or positive. Meaning that in reality, the physical shape and mass of the body within the incompressible control volume remain invariant. The added mass, or added inertia, dominates for a very short time, only during the imposed acceleration or deceleration. After this the flow quickly separates and the viscous effects become prevalent. This imposed acceleration is experienced during pipe movement from a still position. The imparted unsteady motion coincides with the undeveloped region of flow, outlined in section 3.4.

Sarpkaya (2010) also denotes some of the parameters which affects the instantaneous values of drag, lift and any component of the added mass effects. These parameters include, but not limited to, the size, shape, orientation, the path of motion of the body, flexibility of the body, density of the fluid, stratification of the surrounding fluid, dissolved gasses in water, cavitation, separation of flow (vortex shedding, etc.), proximity of other bodies (walls, or a large number of other rigid/deformable bodies), the flexibility, deformability, and surface roughness (size, shape, and distribution of rigid as well as soft excrescences), or free-surface proximity, waves, currents, and internal waves, the prevailing wave and current motion near the free surface, moving from one medium to another (interface between air–water), density stratification, sloshing of liquids inside the body (if any), porosity of the body (the number, size, shape and distribution of holes, hole sizes and their shapes, and pitches.

In Hovda (2018) it was determined that the added mass term is independent of viscosity. The parameter which effected the term the most was the larger diameter strings creating tighter holes with less clearance between drillstring and borehole or casing.

3.3 Basset Forces

The second term in equation 3.6 refers to the basset forces in the model outlined in Hovda (2018). This is a history term predicting the time delay. This delay is due to basset forces which are caused by the lagging response of boundary layers to particle acceleration. The particles experience an unsteady force due to instability of boundary layers Pannala et al. (2011). Since the Basset force depend on the acceleration history up to present time, it is also known as the history force and is defined as the integral of all past particle acceleration. The origin of the Basset force is from the generation of vortices along the particle surface to diffuse into surrounding fluid in order to describe the initial motion of the particle. It therefore constitutes an instantaneous flow resistance which become substantial when the particle is accelerated at a high rate, as seen in Hovda (2018). According to Olivieri et al. (2014) the contribution of this force to the total particle acceleration is, on average, responsible for roughly 10 percent of the total acceleration and particularly relevant during rare strong events. In the work with drag coefficient calculations in Mabrouk

and Guy (2006) the Basset term had a significant impact. It was shown that inn comparison with experimental data the basset forces was especially prominent in low Reynolds number flow.

3.4 Velocity Profile in the Wellbore

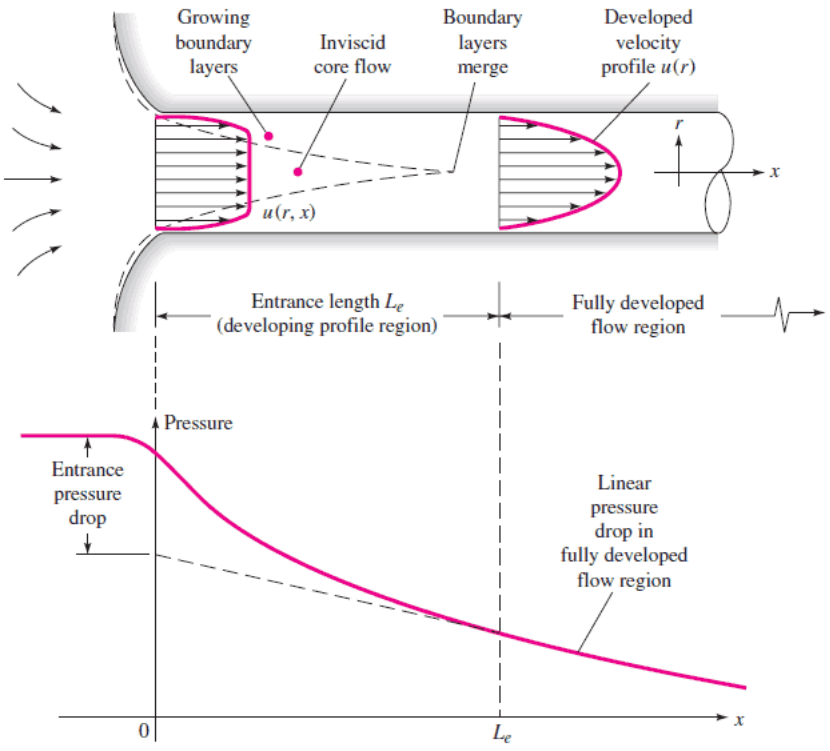

Figure 3.4: Hydrodynamic entrance length and fully developed region with pressure response. Figure from the fluid mechanics textbook White (2010)

During a stationary situation in the drilling process, the pumps may also be shut off. This may be during a pipe connection or other maintenance work. In this situation, the drilling fluid and drillstring is stationary. When the string is then agitated, either by the topdrive or heave-motions of the rig, the drillstring and fluid is accelerated. During the acceleration of the pipe the fluid will either displace the void of the string or be displaced by the string. This flow will have a velocity profile which is not fully developed. The fluid requires a certain length of flow, depending on the geometry and flow, to be fully developed. This development affects the pressure distribution along the wellbore as well as the drag coefficient along the string and casing. The viscous effect is also considerable within the developing boundary layer according to Khalil et al. (2008). The displacement of fluid will due to the no-slip condition require a certain length of movement in order to

become fully developed. As the drillstring is accelerated, the fluid particles along the wall of the casing and string will not move. Due to friction between the particles in adjacent layers , there will be a gradual slowing down of the particles in the annulus from the wall. This in turn creates higher velocity field in the midsection of the annulus in order to have a constant mass flow rate. This boundary surface creates two regions in the annulus , the velocity boundary layer and the invicid or irrotational flow region as seen in figure 3.4. The viscous effects and velocity changes are significant in the boundary layer while the frictional effects are negligible and velocity is essentially constant in the radial direction Cengel and Cimbala (2010). The flow up until it reaches its fully developed state is known as the hydrodynamic entry length denoted L_e. After reaching this state during constant flow, the velocity profile remains constant and the region is hydrodynamically fully developed. The wall shear stress will be highest during the onset of string excitation and fluid flow due to the limited boundary thickness. As illustrated in figure 3.4, the pressure decreases gradually with the growing boundary layer up until the flow is fully developed. The hydrodynamic entry length L_e can be calculated as a function of Reynolds number up until the wall shear stress reaches within 2 percent of the fully developed value Cengel and Cimbala (2010). Expressed for laminar and turbulent flow as

$$\frac{L_{e,laminar}}{D} = 0.05Re \tag{3.7}$$

$$\frac{L_{e,turbulent}}{D} = 1.359Re^{\frac{1}{4}} \tag{3.8}$$

A numerical model of the momentum equation for flow in an annulus with a concentric moving cylinder was constructed in Khalil et al. (2008). The velocity profile development was established for different Reynold numbers, diameter ratios and fluid velocities. The results were verified by the analytical solution of the momentum equation. This model showed that the shear stress and drag coefficient is high during the initial flow illustrated in figure 3.5. With a longer entrance length, the pressure response will be affected by the higher drag and shear stress.

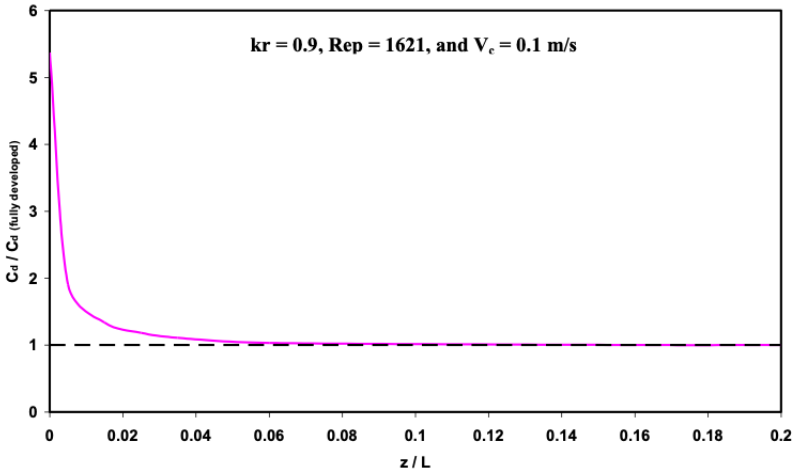

Figure 3.5: Core drag coefficient within the developing region. With diameter ratio, kr, Reynolds number, Rep, and fluid velocity, V_c. From the conference paper Khalil et al. (2008)

3.5 Drilling Fluid Rheology

During drilling operations, a drilling fluid is circulated from surface through the drillstring and bit-nozzles and up the annular space between the drillstring and borehole wall. The drilling fluid serves a number of functions. It cools and lubricates the bit during drilling, provides hydrostatic pressure to counter the pressure in the formation, transport the generated rock cuttings to surface and transmit hydraulic energy to downhole tools Nazari et al. (2010). The three main types of drilling fluids, known as mud, utilized in the industry today are water based mud (WBM), oil based mud (OBM) and synthetic based mud (SBM) Skalle (2011). The desired function of the mud is achieved with the choice of the three base fluids and different additives. The majority of drilling muds express non-newtonian fluid behaviour due to the complex composition of additives.
A **Newtonian fluid** is a fluid that express constant viscosity for any shear strain rate it is subjected to. There is a linear relationship between shear stress and shear strain rate which is stated in Newton's law of viscosity (Cengel and Cimbala (2010)

$$\eta = \frac{\tau}{\dot{\gamma}} \tag{3.9}$$

With shear stress τ, dynamic viscosity η and shear strain rate $\dot{\gamma}$.
Shear stress is defined as the stress co-planar with a materials cross section defined as the force per unit area required to sustain a constant rate of fluid movement defined as $\tau = F/A$ where τ is shear stress given in Pascal [Pa], F is shear force in Newton [N] and A is area given in square meters $[m^2]$.
Shear strain rate is the rate of change of velocity at which one layer of fluid passes over an adjacent layer and is defined as $\dot{\gamma} = v/h$. Where $\dot{\gamma}$ is given in reciprocal seconds $[1/s]$,

v is velocity in $[m/s]$ and h is the shear gap in meters [m]. Shear strain rates during a drilling operation may vary from 10^2 [1/s] in the annulus to 10^5 [1/s] at the bit nozzles (Tehrani (2008)).

Non-Newtonian fluids have a non-linear relationship between shear stress and shear strain rate. Different rheologic models exist in order to describe this relationship depending on the behaviour of the fluid. These fluids may express dilatant (also shear-thickening) behaviour where the apparent viscosity increases during deformation (shearing). Examples of fluids exhibiting this behaviour are solutions with starch or sand. Non-Newtonian fluids may also express pseudoplastic (shear-thinning) behaviour where the apparent viscosity decreases during deformation (shearing). Examples of pseudoplastic fluids are paint and polymer solutions (Cengel and Cimbala (2010)). The behaviour of these fluids are illustrated in figure 3.6a) as well as Newtonian behaviour.

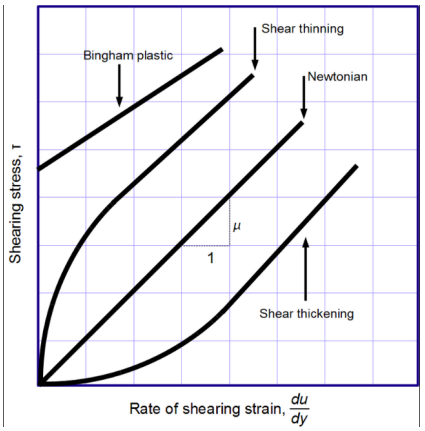

(a) Pseudoplastic (Shear-thinning) and Dilatant (Shear-thickening) Behaviour. "Viscous regimes chart" released into the public domain at English Wikipedia. Dhollm (2017).

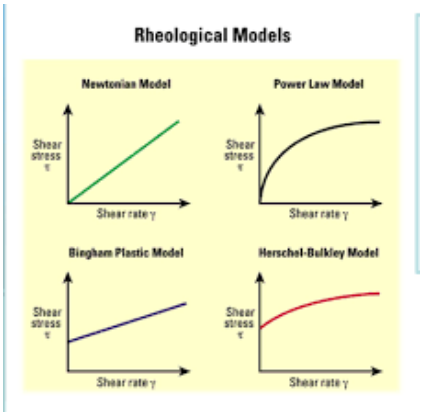

(b) Illustration of different viscosity models. "Rheological models" from SLB Glossary, Gloassary (2017).

Figure 3.6: Fluid Behaviour and Viscosity models

Some fluids require a finite stress in order to flow. This is defined as the yield stress. These fluids have a yield point which is the required shear stress at zero shear strain rate in order to break down the inherent structure of the fluid and make it flow. Fluids exhibiting this behaviour are known as Bingham plastic fluids illustrated in figure 3.6 a)b). Most drilling fluids are not perfect Bingham plastic fluids but many are fairly accurately described by this model, except at very low shear strain rates where it tends to overestimate the yield point (Tehrani (2007)). The Herchel-Bulkley model is a yield-power law (YPL) model wich is derived from the power law and Bingham plastic models, illustrated in 3.6 b). This is a flexible model and when applied to a minimal range of shear strain rates, has a good fitting for a wide range of drilling fluids (Maxey (2007)). The Herchel-Bulkley model is defined as

$$\tau = \tau_y + k * \dot{\gamma}^n \tag{3.10}$$

Where τ is shear stress, $\dot{\gamma}$ is shear rate, τ_y is Herschel-Bulkley yield stress, k is a consistency factor and n is flow index which is a power law exponent.

In order for a drilling fluid to have a cuttings carrying capacity of the generated cuttings as well as solid suspension of weighing materials to increase the density of the drilling fluid, it is desirable for the fluid to form a **gel structure**. Gel structure formation also helps to prevent fluid invasion into the formation and lost circulation problems (Bui et al. (2012). The gel strength is the shear stress measured at low shear rates for a fluid that has been still for a given time. This is set to measurements at 10 seconds and 10 minutes in the API standard. Strong gel indicates that a fluid form a strong associative network that resist breaking when subjected to shear. This behaviour is defined as non-progressive and allows for quick generation of gel strength (Maxey (2007).

Some non-newtonian fluids exhibit a "memory" where the shear rate depends not only on the local strain rate, but also on its history. A fluid which returns, either fully or partially, to its original shape after the applied stress is released is called **viscoelastic** (Cengel and Cimbala (2010). These fluids are time dependant fluids that exhibit both viscous and elastic responses under deformation which allows for evaluation of gel formation and gel structure of drilling fluids (Bui et al. (2012)). The predominant method of determining the viscoelasticity of a fluid is through a dynamic oscillatory test. The fluid undergoes a sinusoidal deformation and the resulting stress is recorded. The two-plate model illustrated in figure 3.7 can be used to describe the viscous and solid like behaviour. A sample is placed between the plates. The lower plate is stationary while the upper plate is moving parallel to the lower plate with a constant oscillating frequency.
The deflection of the upper plate is measured as the shear strain, γ, while the stationary lower plate counters this force exerted through the sample and is a measure of shear stress, τ. During the oscillatory test, the resulting deflection on the upper plate is a sinusoidal strain test with amplitude ,γ_A and period t. The lower plate experiences a similar sinusoidal reading of shear stress with amplitude, τ_A illustrated in figure 3.7.

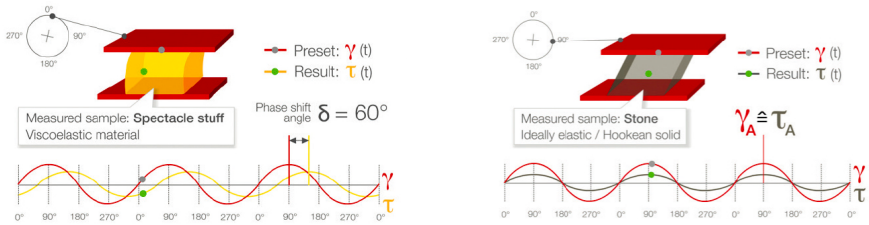

(a) Viscoelastic Fluid Response

(b) Viscoelastic Solid Response

Figure 3.7: Viscoelastic fluid and solid response of dynamic oscillatory test. Figures from Anton Paar GmbH: e-learning course – Basics of Rheometry, Anton Paar (2010)

For an ideally elastic sample, there is no time lag between the two measurements and the phase shift between the two sinusoidal curves $\delta = 0$ degrees. For an ideally viscous flow

behavior, the phase shift is $\delta = 90$ degrees. An example of viscoelastic fluid and solid response is illustrated in figure 3.7.
The total viscoelastic behavior of a sample can be described by the complex shear modulus G^*, also denoted as the Dynamic modulus:

$$G^* = \frac{T_A}{\gamma_A} \tag{3.11}$$

Where T_A is the shear-stress amplitude and γ_A is the strain amplitude of the oscillatory shear test. The complex shear modulus can further be decomposed into two vectors, storage modulus (G') and loss modulus (G'') which is the elastic and viscous component of viscoelasticity respectively. By determining the storage and loss modulus one can express the viscoelastic behavior of a sample. For $G' > G''$ equals a viscoelastic solid while $G'' > G'$ represents a viscoelastic liquid.
The dynamic modulus originates from dynamic mechanical analysis. Where the storage (elastic) modulus (G') measures the energy stored per cycle of the oscillatory test and the loss (viscous) modulus (G'') measures the energy lost per cycle (Bui et al. (2012)).

A oscillatory step test, illustrated in figure 3.8, shows the time dependant functions of the storage (G') and loss (G'') modulus from rest, during deformation and structural regeneration of the fluid. The sudden movement of the drillstring from still position is similar that of the oscillatory step test.

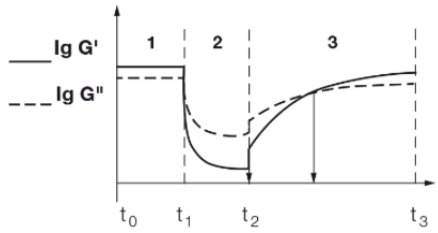

Figure 3.8: Oscillatory Step Test. 1) Solid state at rest with $G' > G''$. 2) Liquid Behaviour with $G'' > G'$. 3) At rest during structural regeneration with crossover point $G' = G''$ and solid state $G' > G''$. From "Time Dependant Behaviour (Oscillation)" article Anton Paar (2020).

Another characteristic common to drilling fluids is its ability to form a gelled structure when not agitated by subjection to shear stress. This is defined as **Thixotropy** and it is a reversible decrease in viscosity in time when made to flow Maxey (2007). The Thixotropic behaviour is generated by flocs or aggregates between suspended particles or moieties in the fluid. For clay suspension drilling fluids the formation of structure is due to increased encounter between particles which can be due to Browinian motion of the particles or from the velocity gradient when the bulk of the fluid is sheared. This Thixotropic behaviour occurs when the net buildup effect is dominant over the breakdown effect of shear Tehrani (2008). According to the DIN (2012) standard, the level of thixotropic behaviour can be analysed through a osciallatory step test as illustrated in figure 3.8. The time the sample uses in order to build structure i.e from shear to $G' = G''$. The analysis can either be recovery after a given time or the time for a given recovery of structure.

Chapter 4

Experimental Infrastructure

The experimental infrastructure was constructed according to the design proposal presented in Sørgård (2019)) with the experimental setup first constructed during the work of Tobro (2018) as basis. The experimental well-setup is fitted within a 100m deep pre-drilled 10" cased hole in the hall building adjacent the Petroleum Technical Center at NTNU in Trondheim, Norway. The experimental infrastructure consists of a 66 meter 3 inch well, 1/2 inch drillstring, 2 1/2" bottom hole assembly and associated sensors. The experimental infrastructure is designed to represent a cased hole where the drillstring is hung of in the slips on a floating rig. By linear excitation, the heave motion induced to the drillstring by the rig is simulated. The new implementations to the setup consists of an axial linear motor, pressure and temperature sensors as well as a larger supporting structure. A full description of the experimental infrastructure is presented in the following sections.

4.1 Casing

The pipe representing the cased well in the experimental infrastructure is re-used from the original setup. The casing consists of eleven 3" , 6 meter pipe sections fitted within the existing 10" well. The pipe specifications are presented in table 4.1. In order to attach the new implementations it was necessary to dismantle the setup due to the location of the new sensors as seen from the design proposal from Sørgård (2019) in figure 4.1. Before assembly, each casing section was visually inspected for any damages or discrepancies before the threads were wire brushed and cleaned with 2-propanol. Loctite 577 was applied to the threads to ensure a proper seal between the sections. Using the installed surface slips, each section was hung of as a new section was lifted in place with the in house 11 ton traverse crane. Each section was tightened using a pipe wrench at approximately 100 Nm of torque. After mounting the entire casing-string it was mounted to the steel garters of the flooring at surface seen in figure B.5 in appendix together with the surface slips. The first section of the casing string consists of the closed end bottom section which is fitted with a T-joint to connect with the flow loop, a pressure sensor, magnetostrictive position sensor rod as well as an air controlled valve on the flow loop outlet. The bottom hole

sensor fittings are seen in figure B.3 in Appendix. The valve was put in place to be able to close the flow loop during testing in order to have the same static functions that of a well. The first casing section also contain tube guides mounted to the wall of the pipe which has the same dimensions as the first drillstring BHA section. These were mounted in order to protect the magnetostrictive position sensor rod at bottom from contact with the drillstring. With an 18 meter spacing, three more pressure sensors were fitted to the casing string as indicated in figure 4.1. These mounts were initially in place during the original version of the experimental setup. The two new temperature sensors were fitted to the casingstring using threaded PVC sleeves between the pipe sections with a steel spacer welded to the casing in order to shield the sensor fitting from contact with the 10" casing during installation. The temperature sensor fitting and spacer can be seen in figure B.2 in appendix. The connections between the sleeve and pipe was fitted with Loctite SI 5331 which is specific for plastic connections. The 1 inch flow loop hose and sensor cables were continuously fed from cable drums and attached to the casing string using zip ties at approximately every 1.5 meter. The sensor cables run parallel to the casing up to surface and follows a cable canal attached to the supporting structure up to the junction box in the second floor above the supporting structure as seen in figure B.21. All sensors, data acquisition system and motor driver are connected here.

Table 4.1: Pipe specifications of drillpipe, BHA and casing

	Serial number	Length [m]	OD [mm]	ID [mm]	Area [mm^2]	Weight [kg/m]	Density [kg/m^3]
Drill pipe 1/2 "	1001207	61.8	21.3	14.9	182.0	1.46	8023.7
BHA 2 1/2"	Smith Staal	6.00	63.5	60.3	311.1	2.48	7990.0
Casing 3"	1001021	66.0	76.2	68.9	820.0	6.63	8058.8

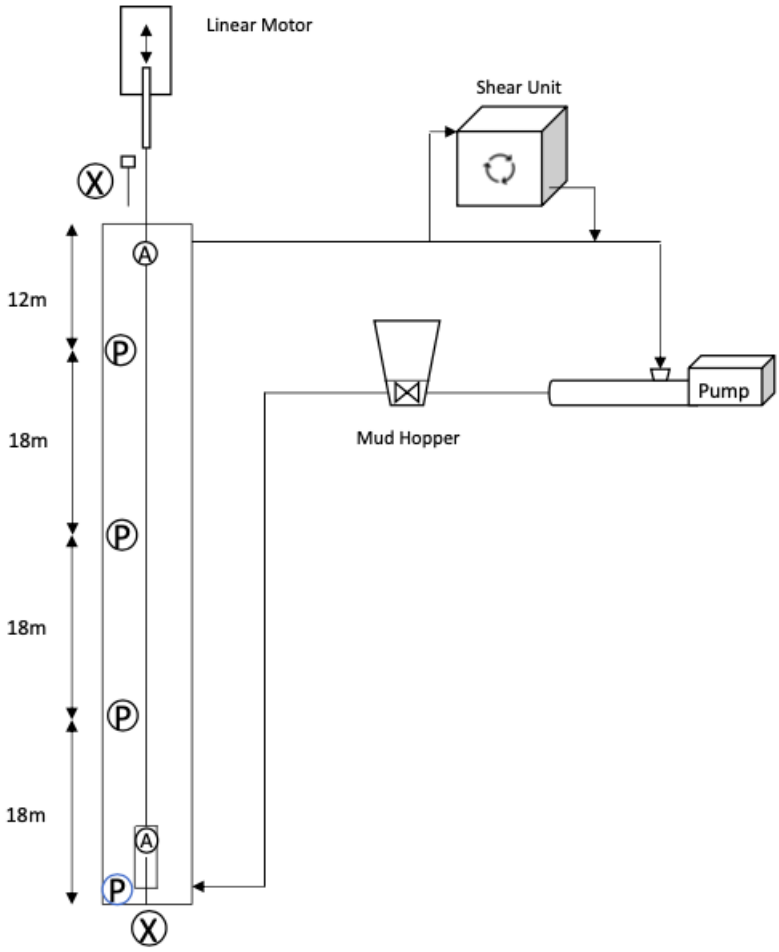

Figure 4.1: Design proposal for experimental infrastructure from Sørgård (2019) with pressure sensors (P), positional sensors (X) and accelerometers (A). Flow loop equipment of original design proposal contain shear unit, mud hopper and progressive cavity pump.

4.2 Drillstring

The drillstring was dismantled and reassembled in the same manner as the casing string. Each section was visually inspected for damages, threads were wire brushed, cleaned with 2-propanol and applied with Loctite 577 before the section was put in place.
The drillstring consists of 12 sections of pipe and total a length of 67.9 meters. The drillstring is designed to approximate the setup of an industry standard drillstring which consists of two sections, the bottom hole assembly (BHA) and drill pipe (DP). In a drilling operation, the BHA is the lower portion of the drillstring consisting of the bit, drill collars, heavy weight drillpipe and various tools for directional steering and logging. The BHA is required to endure tremendous stress and a hostile environment. This requires the use of high grade steel and larger diameter pipe. The BHA in the experimental infrastructure was constructed using a 2 1/2 inch AISI 316L stainless steel delivered by Smith Stål. A non-magnetic steel alloy containing chromium was chosen to avoid any interference with the magnetostrictive sensor at the closed end bottom section of the casing. The bottom of the BHA was fitted with a 10 centimetre brass funnel acting as both a drill bit as well as a guide for the bottom hole sensor rod. This can be seen from the figure B.6 and schematic B.7. The drillpipe was fitted to the BHA through a rounded crossover (figure B.8) to help guide it through the well. The first section of drillpipe was 1.8 meters long in order for the pipe connections of the drillstring to be shifted from connections of the casing sections. This is due to the risk of the connections snagging during axial displacement during experiments. The drillpipe is a 1/2 inch stainless steel pipe grade S195 provided by Ahlsell. The pipe specifications of the BHA and DP are listed in Table 4.1.

The full setup of the drillstring consisting of the BHA and DP is illustrated in figure 4.2. In this figure, the intermediate drillpipe sections have been excluded for illustration purposes ,since they have equal pipe specifications. With the current setup the drillstring stands approximately 1.8 meters above surface where it is connected to a slide block on the supporting structure further explained in section 4.5. A full overview of the drillstring pipe specifications is given in table 4.2. With the current ratios between DP and BHA outer diameter to casing inner diameter, assuming DP represents a 5” outer diameter DP, the resulting BHA represents a 14,9” outer diameter with a 16,70” casing inner diameter. This hole size is common in the intermediate sections of a well. Though the annular gap between the BHA and casing is more commonly experienced in the deeper parts of a well.

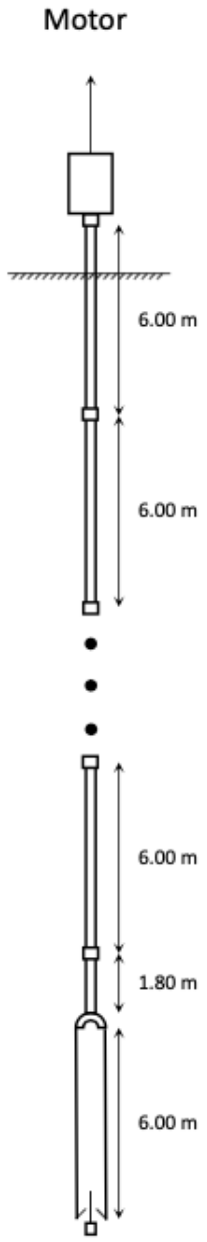

Figure 4.2: Illustration of drillstring setup with drillpipe and the bottom 6.0 m BHA. Figure not to scale for illustration purposes.

Table 4.2: Specifications of drillstring components

Joint Nr.	Type	Length [m]	OD [mm]	ID [mm]	Weight [Kg/m]
1	1/2" DP	6.00	21.3	14.9	1.46
2	1/2" DP	6.00	21.3	14.9	1.46
3	1/2" DP	6.00	21.3	14.9	1.46
4	1/2" DP	6.00	21.3	14.9	1.46
5	1/2" DP	6.00	21.3	14.9	1.46
6	1/2" DP	6.00	21.3	14.9	1.46
7	1/2" DP	6.00	21.3	14.9	1.46
8	1/2" DP	6.00	21.3	14.9	1.46
9	1/2" DP	6.00	21.3	14.9	1.46
10	1/2" DP	6.00	21.3	14.9	1.46
11	1/2" DP	1.80	21.3	14.9	1.46
12	Cross Over	0.025	N/A	N/A	N/A
13	1 1/2" BHA	6.00	63.5	60.3	2.48
14	Cross Over	0.01	63.5	15.0	N/A
15	Funnel/Bit	0.1	66.5	32.6	N/A

4.3 Progressive Cavity Pump and Flow Loop

The original progressive cavity pump is being utilized to power the flow loop in further experiments. The pump installed is a Wangen Kl-30S delivered by Froster Prosesspumper og Engineering. It has a pumping capacity of $9m^3$/h at 161 RPM. It is rated for a differential pressure of 48 Bar. The progressive cavity pump, illustrated in figure 4.3, is based on the same design as a positive displacement motor (PDM) used in drilling operations. The difference being that instead of mud flow to power the rotor, it is powered by an electric motor unit. The rotation of the rotor within the stator creates the pumping effect and the direction of flow is as indicated in figure 4.3. The current experiments with the new experimental infrastructure is limited to water and static fluid in the well. Therefore the full flow loop is not active. In future experiments, the pump will be connected to the flow loop running parallel with the casingstring, pumping down the outside. The top T-section will be connected to the flow loop running to the reservoir tank. This is a 1 m^3 IBC tank which will then be connected to the pump inlet as indicated in figure 4.1 where the tank is denoted Shear Unit. The indicated mud hopper is currently not a part of the new design as there are is a mixing tank within the lab.

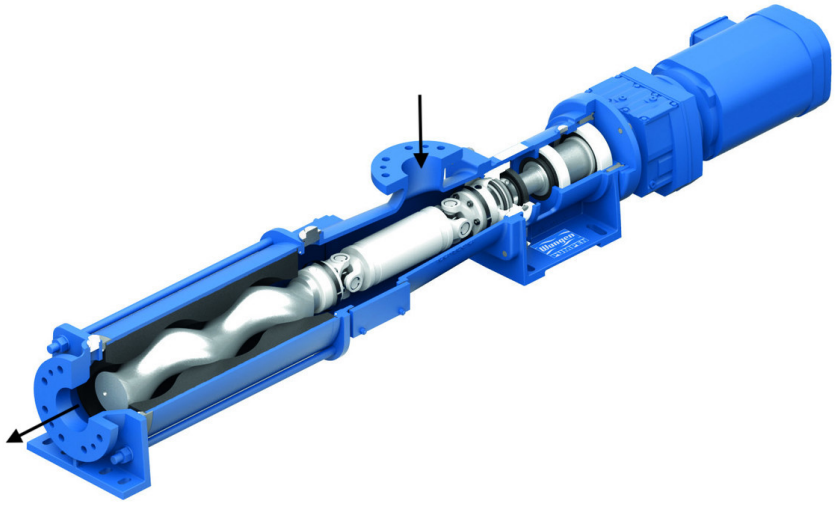

Figure 4.3: Wangen KL-30S Progressive Cavity Pump with indicated in- and out-flow direction. From ”Progressing Cavity Pumps KB-S/KL-S” data sheet, Pumpen (2020)

4.4 Well and Drillstring Sensors

Several sensors are fitted to the experimental infrastructure. These sensors are mounted to accurately measure the induced pressure and temperature variations caused by excitation of the string which is accurately monitored by displacement sensors. The new experimental infrastructure has one less magnetostrictive positional sensor compared with the previous setup. This is because the linear motor unit has an inherent measuring of excitation. The sensor specifications and functions are listed below.

4.4.1 Magnetostrictive Linear Position Sensors

In order to monitor the exact excitation of the drillstring during experiments, an axial magnetostrictive positional sensor rod delivered by Balluf is mounted to the closed end casing bottom. As presented in Sørgård (2019), Magnetostrictive sensors rely on a materials magnetoelastic properties to convert a physical parameter of interest into an electrical dimension that can be processed and transmitted (Calkins et al. (2007)). Some sensor systems use the inherent magnetoelastic property of the target while other sensor configurations use the magnetostrictive properties of the part of the the sensor itself to measure the property of interest. The latter is used in this experimental infrastructure. These sensors are designed with a housing containing processing electronics and a sensor rod transducer containing a waveguide within. The sensor rod consists of two parts, the nominal length and the damping zone. The sensors utilize the torsional waves in the waveguide of the sensor rod to measure the position of a magnet in the drillstring. This is made possible by utilizing the ferromagnetic properties of the sensor material as the presence of a magnetic

field causes the material to change physical properties. a short current pulse is transmitted from the sensor element creating a momentary radial magnetic field. the momentary interaction between the radial magnetic field and the magnetic field of the magnet in the drillstring releases a torsional strain pulse that propagates the length of the waveguide. The ultrasonic wave is transformed into an electric signal in the housing and dampened in the damping zone to avoid reflection as illustrated in figure 4.4. Since the inherent velocity of an ultrasonic pulse is known, the distance can accurately be determined.

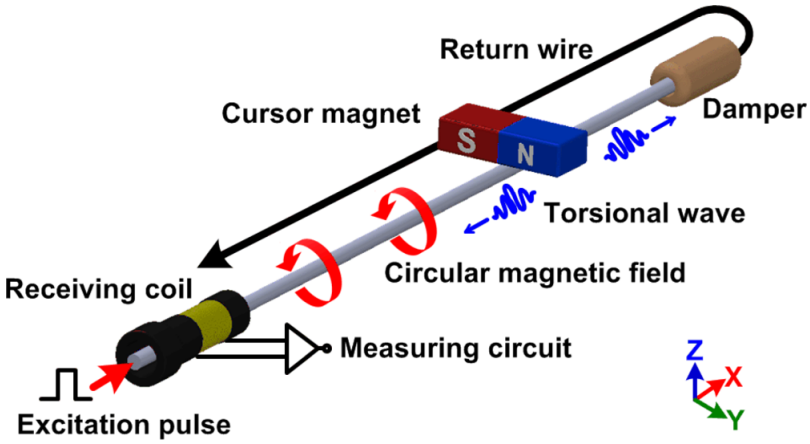

Figure 4.4: Magnetostrictive linear position sensor illustration. Figure from paper on differential waveguides, Zhang et al. (2011)

The magnetostrictive sensor was mounted to the closed end casing bottom to accurately determine the position of the drillstring during experiments. The sensor rod installed measures 1000 mm and is centered within the BHA.

The sensor from Balluf is designed and intended for use in pressurized hydraulic environments. This is necessary for fluid filled well measurements with different fluids. The installed sensor is shock and vibration resistant so that it can withstand any induced shocks from the drillstring. Since the bottom section of the casing contains guides for the BHA, there will not be any direct shocks from the drillstring but the drillstring may induce shocks and vibrations to the casing itself which the sensor is mounted to. There may also be vibrations of the casing from the motor assembly.

The analog output of the sensor range from 4-20 mA, where 4 mA equals zero displacement and 20 mA equals the 1 meter measuring length of the sensor rod. A scaling from the analog output signal from the sensor to a digital measurement is accomplished by use of the graphical programming tool LabView. A scaling is necessary for the sensor and is presented together with the sensor specifications listed in table 4.3.

Table 4.3: Balluf Magnetostrictive Sensor Specifications

Placement	Bottom Sensor
Product name	BTL7-E100-M1000-B-KA-05
Measuring Length	1000 [mm]
Pressure Rating	600 [bar]
Max Sampling Frequency	1000 [Hz]
Analog Output	4 - 20 [mA]
Operating Voltage	24 [V]
Repeat Accuracy	$\pm$ 5 [μ m]
Conversion Scale	f(x) = 62.5X mm/mA + -250 mm

4.4.2 Acceleration Sensors

An attempt was made to fit the drillstring with accelerometers during construction of the experimental setup in Tobro (2018). These sensors did not function as originally intended and were not fitted to the original setup. In the new experimental infrastructure, accelerometers are redundant as direct measurements is achieved through the linear motor and magnetostrictive sensor rod.

4.4.3 Limit Switch

Two Honeywell SZL-VL-S-B-N-M Miniature industrial limit switches have been fitted to the supporting structure, visible in figure B.20 in appendix. The switches were mounted in order to make sure that the vertical excitation of the string from the motor does not exceed the 1000 mm measuring length of the magnetostrictive sensor rod. The switches are shock rated at 30G and vibration rated at 10G which make them ideal for use in the experimental infrastructure as shock and vibration is expected to be considerably less.

4.4.4 Pressure Sensors

In order to accurately quantify the induced pressure variation due to surge and swab, three pressure sensors were installed along the wellbore in the initial experimental setup. These sensors are of the UNIK 5000 series pressure sensors from General Electric. The sensors are 12 bit sensors with an operating range from 0 to 10 bar with a sample frequency of 80-100 kHz and a sensitivity of 0.15 mBar. A new GE Druck PTX57N2 titanium submersible pressure transmitter supplied by Tormatic was installed in the new experimental infrastructure. This sensor is of the UNIK 5600 series which has the same specifications as the previously installed senors. This sensor was installed at the bottom of the casing to monitor variations of the bottom hole pressure during drillstring excitation. The placement of the pressure senors along the casing is illustrated in the sensor overview in figure 4.5.

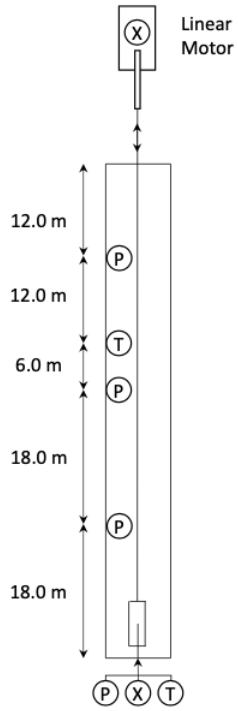

Figure 4.5: Location of sensors along the well in the experimental infrastructure where X, P and T denotes positional, pressure and temperature sensors respectively.

4.5 Axial linear motor and supporting structure

The installed driving force motor is a linear motor supplied by NTI AG Linmot and Magspring with a stroke length of 1130 mm as seen from figure 4.6. This allows for some adjustment as the magnetostrictive sensor rod has a measuring length of 1000 mm. The installed motor has a 3x400v/28A Linmot IP servo drive which allows for integration of the linear motor with industrial ethernet interfaces. The servo drive has a transfer rate of 10/100 MBit/sec. The linear motor has non-contact, integral position feedback which makes a top positional sensor redundant. The position output from the motor is per industry standard 1 Vpp Sin/Cos signal with 40 mm period. The output is in the form of analogue, differential sine and cosine signals. This output relationship is illustrated in figure A.3 in appendix. The motor has a electromagnetic direct drive which has minimal wear and does not require intermediate coupling like a mechanical gearbox. The motor consists only of the stator and slider as seen in figure 4.6. The stator consists of motor winding, bearing for the slider, position capture sensors and a microprocessor circuit for monitoring the motor. The slider rod is made from a high precision stainless steel tube which contains neodymium magnets in series. The position capture sensor measure and monitors the cur-

rent position both during motion and stationary. The motor in use has a peak force of 2180 N and a maximum velocity of 4.9 m/s. Additional technical specifications are listed in figure A.2 in appendix.

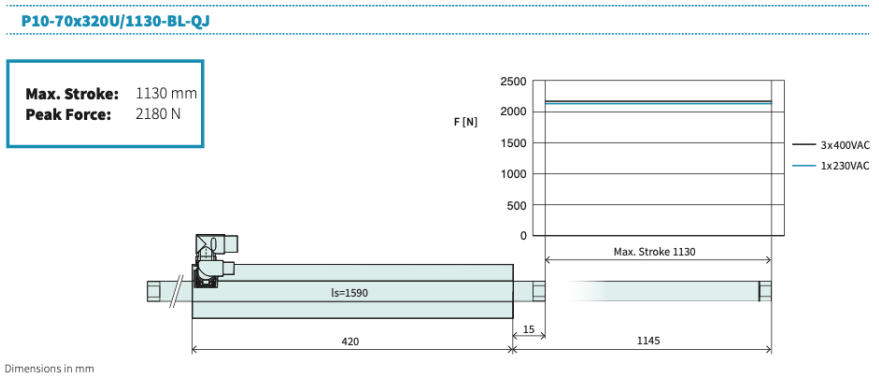

Figure 4.6: Linmot linear motor P10-70x320U stator and slider dimensions. Figure from ”Linear Motors P10-70x320U” data sheet, LinMot (2020)

With the implementation of the new linear motor, a new topside design was made. The linear motor was mounted vertically to the setup in order to connect with the drillstring. It is favorable to have as little static tension on the motor as possible. This would make the motor have a constant load and could lead to overheating and trouble having a consistent movement. Additionally, since it will displace a lower load it will make adjustments easier for operators. Thus, the weight of the entire drillstring has to be supported through the linear motor. This was achieved by having a counterweight attached to the upper end of the slider as seen in figure 4.7. The counterweight is made up by a 3 meter S355J2 AR conditioned micro alloyed structural steel cylinder. The cylinder is fitted with square plastic end fittings to act as a guide providing stable movement within the supporting structure. A groove is machined in the counterweight and end fittings to accommodate the weld line within the supporting structure in order to prevent snagging during experiments. The counterweight is fitted with a 1/2 inch steel chain that runs through a steel cogwheel mounted at the top of the structure through two ball bearings. The other end is mounted to the top of the linear motor as seen in figure 4.7. The linear motor is mounted to a mounting-plate as seen in figure B.14 to the supporting structure in B.15 in Appendix. The connection between the linear motor and drillstring is a slide block mounted to the guide-rail, B.16, attached to the supporting structure. Detailed figures of the motor assembly and supporting structure can be seen in figures B.17 to B.22 in appendix.

After the motor assembly and counterweight was put in place, a 2 inch thick plexiglass protector was fitted to the steel structure between the slider and supporting structure. The slider rod has several strong magnets within the tube and create a strong magnetic field. This may potentially make the slider be attracted to the steel structure and damage both the motor and slider. The plexiglass protectors were therefore attached to prevent any deviation during the linear motor stroke.

The motor is attached to the data acquisition system (DAQ) through connectors at the top of the motor. The cables run through the cable channel together with the sensory cables to the DAQ.

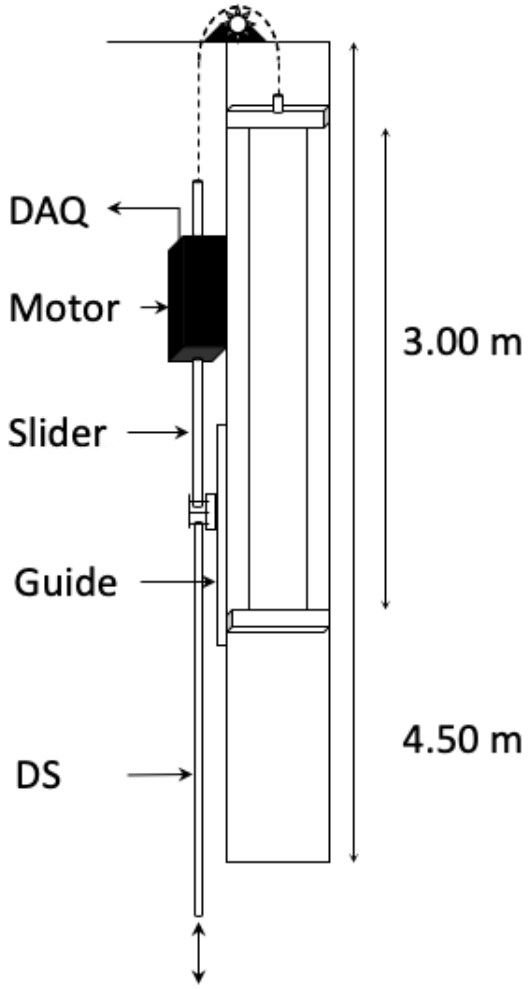

Figure 4.7: Supporting structure for linear motor, counterweight and guide where the motor slider is connected to the drillstring through the slide block attached to the guide. Motor signal cables run to the data acquisition system (DAQ)

4.6 Communication Driver and Module

Communication with sensors and motor was achieved by use of the LabView software. All information from the sensors in the well was routed through a data acquisition system, DAQ, that converts analog signals to digital. The DAQ NI USB-6218 from National Instruments control the synchronization between input and output from the module connected to the sensors and the computer used for processing the data. The linear data from the linear motor is routed through the LinMot E1400 modular axis servo drive. The driver has 32-bit position resolution and an integrated power stage 3x400VAC. Further details are presented in the flow chart in figure A.4. The entire system of sensors and motor control is run through the junction box in figure 4.8

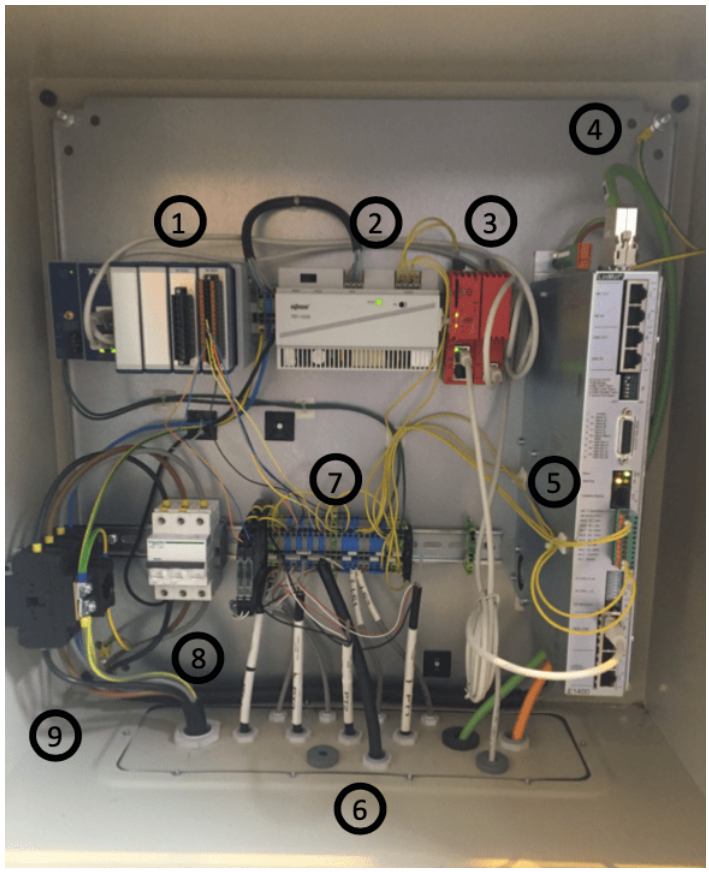

Figure 4.8: Junction box components: 1. DAQ NI USB-6218 data acquisition. Analog input sensor data to digital , 2. 24v power supply , 3. Modbus ethernet/IP gateway , 4. Ground cable for cabinet in case of creeping current from any of the components, 5. LinMot E1400 Servo Drive communication module for linear motor, 6. Cable entry for sensor, motor in feed inlet cables, 7. Distribution of sensory cables , 8. Power fuse of 400 Volt/32 Ampere inlet power, 9. Inlet power main switch

4.7 Flow Loop

The intended flow loop is made from a 25mm rubber hose that is connected to the progressive cavity pump, where it runs from the outlet of the pump down parallel with the casing to the bottom. At the bottom of the casing it is fitted to a T-joint through an air actuated valve. The valve is fitted to the flow loop to have the ability to close the loop during static experiments. The 66 meter inside of the casing, representing the well, makes up the largest part of the flow loop. At the top of the casing there is another T-joint, seen in figure B.5, where the hose is to be connected to the brass outlet and run into a holding tank. The holding tank is a 1 m^3 IBC container which is fitted with hose fittings to be a part of the flow loop. From the tank it runs to the pump inlet completing the flow loop.

The complete flow loop is ready to be connected but will for the time being remain unconnected due to experiments being limited to water during static conditions. The finalized design of the experimental infrastructure is illustrated in figure 4.9.

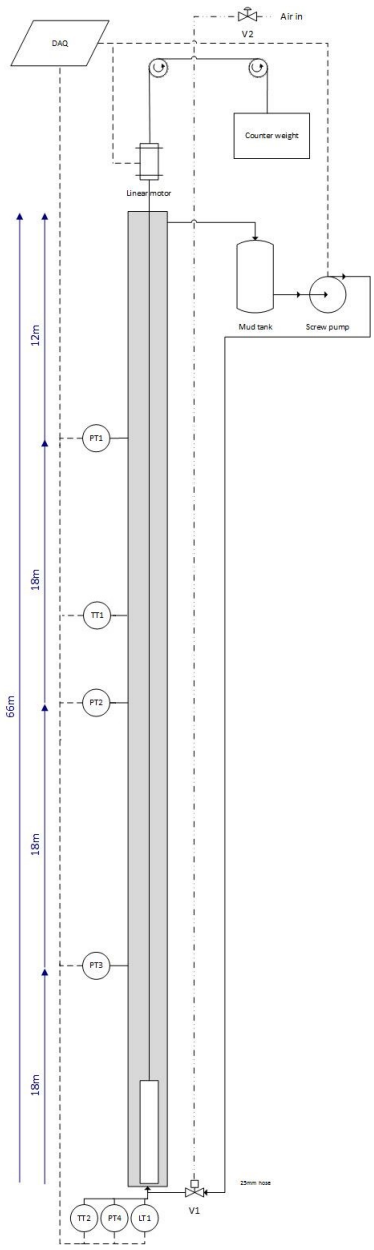

Figure 4.9: Final design of experimental infrastructure where PT, TT, LT denotes pressure, temperature and positional sensors respectively. V denotes valves and DAQ is the Data Acquisition system with additional cables from the linear motor and pump. Linear motor is attached to the LinMot drive adjacent the DAQ within the junction box. The flow loop is indicated from the mud tank and screw pump to the top and bottom of the casing with the air controlled bottom hole fluid vale V1 on the flow loop controlled by air valve V2 at surface.

Chapter 5

Design of Experimental Infrastructure

The new experimental infrastructure was designed to be able to replicate an actual surge and swab situation which is encountered in the industry today. In order to achieve this the axial range of motion has been extended to 1000mm to accommodate a variety of different situations. As surge and swab is encountered whenever the string is moved within the well, it is favorable to have the ability to test different scenarios. The design of the experimental infrastructure is founded in its scientific relevance and practical feasibility. The ultimate goal is to have an accurate experimental rig to determine the pressure variations caused by string movement in a fluid filled well. These pressure variations are defined as the increase (surge) and decrease (swab) in pressure due to string movement.

In a typical drilling operation, the standard diameter of drillpipe in the industry is five inches. The BHA can be of different diameters as it depends on the tools and equipment in use. The implications of pressure variation becomes more significant at larger depths. Here the annular clearance between the BHA and casing or formation is very low which in turn yields a larger pressure variation with string movement Crespo et al. (2012). Due to this the chosen BHA outer diameter is set to 2 1/2" making the annular clearance 2.7 mm. If the drillpipe in the experimental infrastructure is assumed to represent 5" pipe, then with the given diameter ratio the BHA represents 14,9" pipe and the inner diameter of the casing equals a 16.7" casing inner diameter. This sized pipe is common that of the midsections of a well but the annular clearance between the BHA and casing is similar to that of deeper sections of a well or with casing insertion. With the installed magnetostrictive sensor rod at the bottom section of the casing, guides for the BHA have been mounted on the casing wall. These are put in place to assure there is no contact between the BHA and sensor rod. Additionally this will assure accurate measurements from the magnetostrictive sensor. The drawback with this design is that the entire casingstring has to be disassembled if a different BHA diameter is desirable i future experiments.

The ground foundation of the experimental infrastructure consists of large steel tubes to which the entire experimental infrastructure is attached to apart from the casing string. The foundation is designed to be highly robust in order to inhibit any vibrations imposed to it from the drillstring and motor assembly during experiments. To achieve this the foundation is made of heavy stainless steel tubes as well as being mounted to the concrete floor through expandable drop-in concrete anchors at all four corners of the structure. The foundation was placed so that the motor assembly would be directly above the casingstring. In order to have the possibility of adjusting the motor assembly, grooves were cut in the mid section of the foundation, seen in figure B.13. The top and bottom section is then attached through eight 16mm bolts which allows for easy adjustment if necessary.

The supporting structure for the counterweight and motor assembly is attached to the foundation through four 12 mm bolts instead of welding it to the structure. This solution was chosen so that the setup is easier to dismantle if adjustments are necessary or the drillstring is to be replaced. There are pre-drilled holes at different levels in the guide tube for the counterweight where locking pins can be attached. These were made to be able to set of the weight in order for the motor to be detached from the chain connecting the two. Even though the bottom section is bolted to the frame, the top section is welded to the scaffolding structure through a crossbeam. Welding was chosen here over a bolted connection since it would interfere with the travel of the counterweight within the guide tube. The weld is put on top of the crossbeam so that it can easily be ground off using a angle grinder if the guide needs to be dismantled.

The linear electromagnetic direct drive motor was chosen due to its high accuracy movement, stroke length and minimal wear. The non-contact integral position feedback controlled by the servo driver has a minimal cycle time for the position control loop of 125 μs which gives a possible sampling rate of 8000 positional data points per second. This together with 1130 mm stroke length and 4.9 m/s velocity allows for an array of different experiment options. The E1400 servo drive was easy to integrate and operate. With its inherent software it is possible to set predefined control sequences and implement field data for experiments. The motor has a peak force of 2180 N which would allow for the motor to take the full weight of the drillstring. The counterweight was attached so that the motor would not have to be engaged at all times which could result in overheating or the requirement of a cooling unit. The most important reason for having the motor in a neutral position is the possibility of a power outage. If the motor was supporting the full weight of the drillstring, it would drop to the bottom due to the power outage which could result in damage to other equipment or in the worst case people.

A magnetostrictive positional sensor was attached to the bottom casing section. This was mounted due to its high accuracy measurements and relative ease in implementation. As it only requires a magnet within the BHA to measure the position. A drawback with this kind of rod sensor is the necessary guiding of the BHA within the casing in order to shield the sensor. This makes a change in BHA diameter a more tedious task. A challenge with only having one magnetostrictive senor at bottom and relying on the motor position output at surface is the different interfaces between the two measuring systems. Correlating the exact position in time is more complex in order to have an accurate description of the full string movement.

Chapter 6

Preliminary Experiments

A total of three step test experiments were conducted. The initial tests were conducted in order to confirm proper function of the experimental infrastructure and sensors. The three experiment were conducted with the same parameters and stroke length in order to confirm the results as well as determining the accuracy from the sensory equipment. The positional data from the linear motor and magnetostrictive sensor rod was implemented into Excel to be able to investigate the anticipated delay between the top and bottom of the drillstring. The total length of the drillstring is 67.8 metres and with a transfer speed of 5790 metres per second through stainless steel, the anticipated delay between top and bottom should amount to 11.57 milliseconds. This will account for the travel time trough steel in air.

The initial experiment illustrated in figure 6.1, yielded a time delay of approximately 30 milliseconds between the sensor response at top and bottom. This is visible when the plot is scaled to a 100 millisecond time range as seen in figure figure 6.2. This time delay result was consistent in all the initial tests as seen in figures D.1 to D.5 in appendix. The pressure response is plotted in the data acquisition program LabVIEW raw data interface seen in figure 6.1. The pressure transducer (PT) legends PT1 and PT2 have been switched in the plot. The red line plots pressure transducer PT1 pressure response and the dark blue line plots the pressure response of pressure transducer PT2. The pressure response correlates with the drillstring excitation during the step test with a pressure peak of 0.5 bar in the three bottom sensors, PT4, PT3 and PT2.

During the initial experiments the vibrations of the drillstring was visible in the string as well as in the linear motor. With the length and diameter of the drillstring, this was anticipated. The vibration transferred to the motor was minimal and the results from the positional sensor did not show any implications with this vibration. The delay between the positional sensors is not fully accounted for. The estimated delay is 11.57 milliseconds for stainless steel in air. The remaining 20 millisecond delay might be due to the compressibility of the fluid and string. The narrow annular gap between the BHA and casing, the crossover from drillpipe to BHA and several fluid parameters as presented in chapter 3. Further testing is necessary in order to quantify the physical effects affecting

the measurements.

The results from the initial testing shows that the sensor response has the intended high accuracy where the positional sensor data are within the expected range. The pressure fluctuation of the middle pressure transducers is currently unaccounted for. Further testing will be necessary to explain this behaviour.

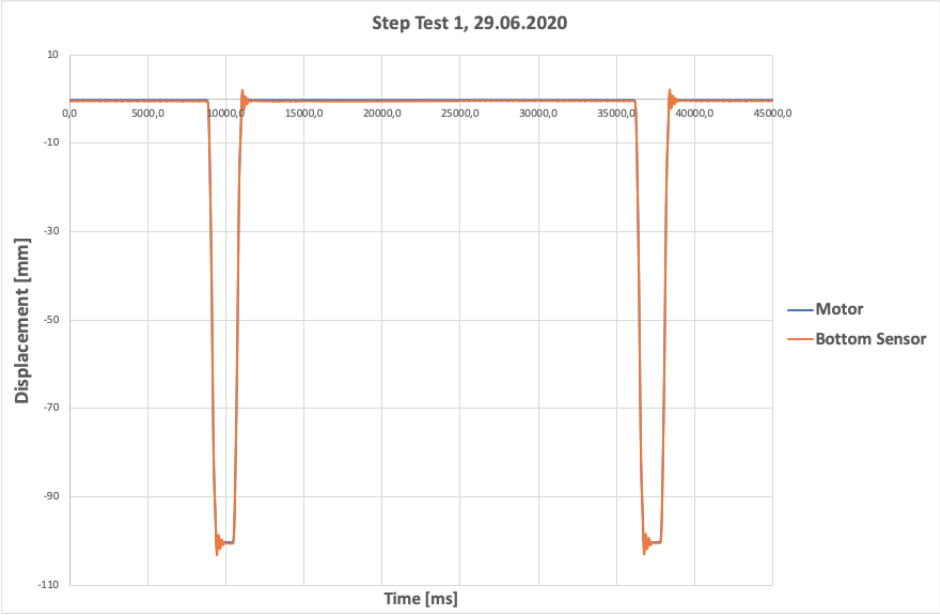

Figure 6.1: Step test 1 positional sensor data from linear motor and bottom hole magnetostrictive sensor rod. Total test time set to 45 seconds. Stroke length set to 100 millimetres.

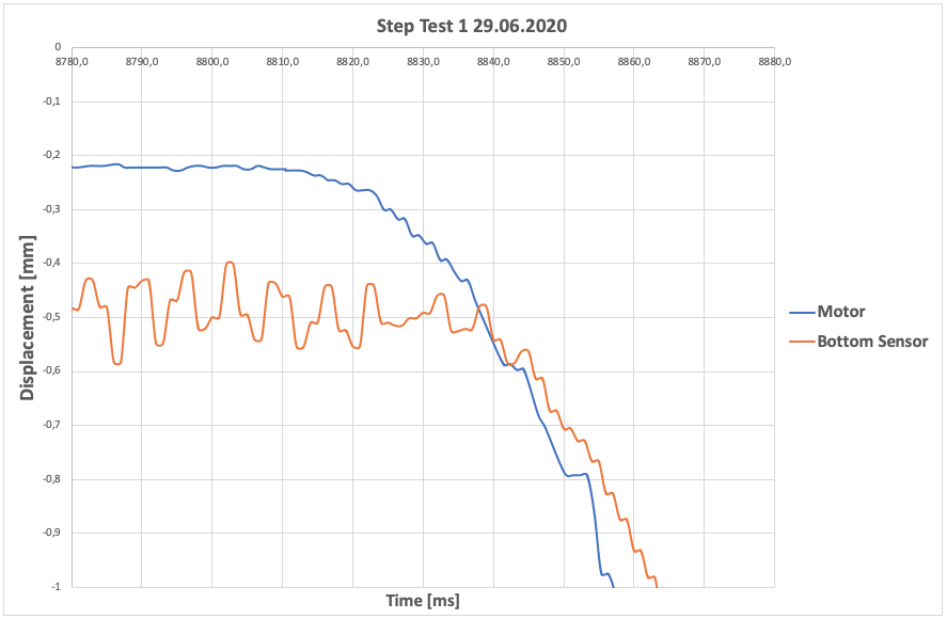

Figure 6.2: Step test of experimental infrastructure. A scaled plot of the difference in motor sensor positional data and bottom hole magnetostrictive sensor rod data. Delay equals approximately 30 milliseconds.

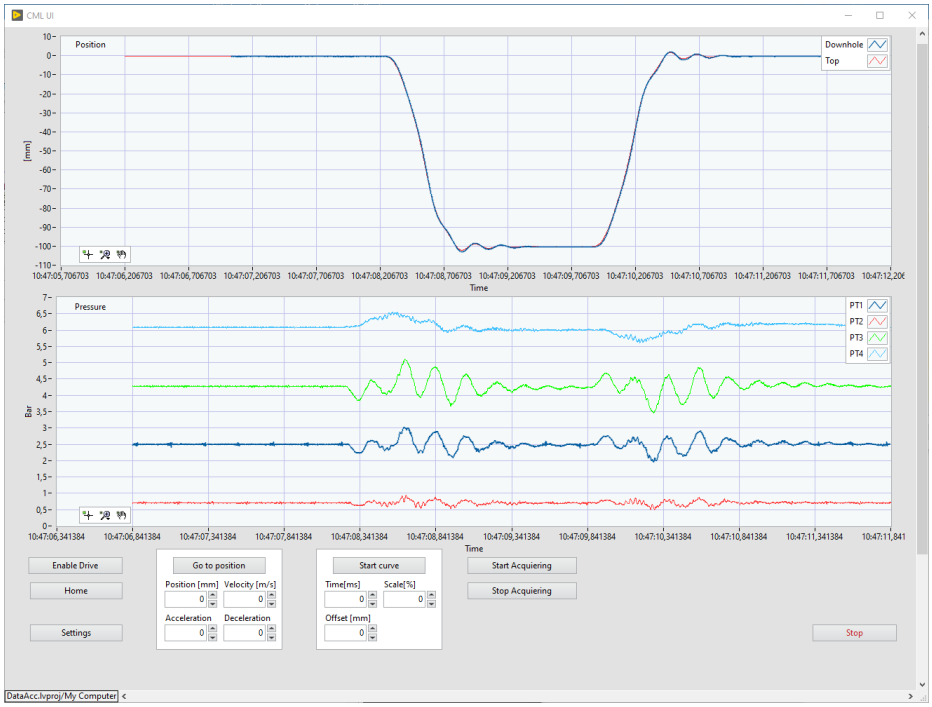

Figure 6.3: Step test 1 raw data from the data acquisition program LabVIEW. Top plot indicating positional sensors. Bottom plot indicating pressure sensor response. Error in labeling, PT1 and PT2 legend is switched. Red line is PT1 and dark blue is PT2. Sensors responding to the movement of the drillstring. Measured surge and swab pressures equal approximately 0.5 bar

Chapter 7

Discussion

An experimental infrastructure for investigating the dynamical effects of surge and swab was constructed. The initial planning and design made it possible for an efficient construction process. Some obstacles arose during construction but was quickly mitigated by the expertise of the senior engineers and mechanics at NTNU. The experimental infrastructure shows great potential for benchmarking surge and swab models. With the current setup it is possible to conduct a wide variety of experiments with different stroke lengths, reciprocal movement and velocities. The flow loop and mixing tank allows for an uncomplicated exchange of drilling fluid within the well. With the downhole valve it is possible to close the flow loop during experiments to have a closed end well.

The initial experiments conducted was through several step tests to verify the sensory output and accuracy. Three step test experiments was conducted with a stroke length of 100 millimetres. The tests had the same input and had correlating results. The sensory output from the magnetostrictive sensor rod and linear motor positional sensor was very accurate and a delay of approximately 30 milliseconds was seen between the two. The analog output of the magnetostrictive sensor was observed to be more erratic, compared to the motor sensor, when investigating the difference in initiation of the axial movement. This was expected as the motor senor has a digital output. The installed temperature sensors was not tested. This was due to the prioritization of the positional and pressure sensors. In order to implement the sensory output, extensive programming is required through LabVIEW in order to process the data from the sensor. Comparing the data from the positional sensors proved to be a bit tedious and required substantial programming in order to present the data together. A consideration should be made in the future of installing a second magnetostrictive sensor rod at the top of the experimental infrastructure. This will allow for easier interpretation of positional data as both sensory outputs will be processed by the DAQ and presented in the same format.

Some vibrations was experienced during initial testing. This was primarily in the drillstring which was expected due to the length of the string. Some vibration was seen propagating to the linear motor but to a limited degree. There is not any mechanical implications

with the vibrations, but it may affect the sensory output from the motor. This was not experienced in the initial testing. Several velocities and stroke lengths were tested to confirm proper function before sensory data was obtained. Due to the limited amount of experiments conducted, there is still some uncertainty in the measurements. The uncertainties lay within possible delays in the system and sensor function.

In the previous experimental setup there was an unexplained delay between top and bottom sensory data. This has yet to be confirmed for the current experimental infrastructure, but the initial tests looks promising as the delay is approximately 30 milliseconds as seen in figure 6.2. With the new setup it is no clear that the same delay will be experienced as BHA diameter is larger and the stroke length and frequency is substantially different from the previous experimental setup. This makes the previous results obsolete and rigorous testing of the new experimental infrastructure is required.

Due to the Covid-19 outbreak, the project was severely delayed which has led to a limited amount of experiments. In order to confirm the functionality of the experimental infrastructure, several tests need to be conducted. This is to assure that the sensory output is within the physical range of what is expected. Once this has been confirmed, experiments with different stroke lengths and speeds needs to be conducted in order to generate a model for the setup. Only after extensive testing of the experimental infrastructure will it be possible to start conducting experiments with drilling fluid representatives with rheologic parameters. In order to be able to quantify the physical effects of rheology on surge and swab pressures, an incremental approach should be conducted. In the preceding work in Sørgård (2019) it was proposed to utilize glycerine as the new experimental fluid. This is due to the physical behaviour of this fluid, as it has viscosity and a linear viscosity profile making it a Newtonian fluid. This way it will be possible to investigate viscosity in its entirety before testing with non-Newtonian fluid commences.

Chapter 8

Further Work

The experimental infrastructure constructed in conjunction with this thesis shows great potential as the excitation force can be regulated with great accuracy through the linear motor as well as the responding pressure variations monitored by the high accuracy pressure transducers. In further work, a comprehensive data processing program should be generated in order to have an accurate comparison and presentation of data. With this in place additional experiments should be conducted with the current setup where the well is water filled in order to distinguish the effects of string movement causing the surge and swab effect and implementing the lumped mass element model created in Hovda (2018). After results are obtained from experiments with water as the well fluid, the drilling fluid proposed in Sørgård (2019) should be added to the system. A comprehensive study on drilling fluid rheology was conducted where selected water based fluids containing Xanthan gum and Glycerol were tested. The proposed drilling fluid additive to be tested was a glycerine solution with 80 wt- $\%$ glycerol content, denoted glycerine-80. This glycerine drilling fluid will only ad the property of viscosity to be accounted for as it behaves as a Newtonain fluid as apposed to Xanthan gum. This was established through experiments conducted in Sandahl and Sørgård (2019) where glycerine-80 have a linear response during a flow curve test as seen in figure C.1 and C.2. The new setup allows for different kinds of experiments as direct heave motions can be applied as well as sudden drillstring movement. This will allow for rigorous testing and improvements to the lumped element model.

When the model has been established and validated by the experimental infrastructure, the next step in testing should be non-Newtonian fluids as they pose an array of new characterisation in order to properly describe the fluids effect on the surge and swab.

8.1 Validation

After the model has been established from experiments using the experimental infrastructure it should be validated using field data. It is believed that with the scale and setup of the experimental rig, that it will be scalable to an actual drilling rig. A possibility of validating the model is using data from the high pressure high temperature (HPHT) sensor in the blow out preventer (BOP) stack as part of the lower marine riser package (LMRP) with heave motion data. In a typical deepwater BOP configuration as seen in figure 8.1, the HPHT sensor is situated below the lower port choke line inlet as indicated by the arrow. With the new experimental infrastructure it is possible to implement the exact heave motion data from a rig and applying it with set ratios to the linear motor. By using a sample of the mud from the operation where data was collected, it is possible to recreate the conditions during heave. Though the pressure and temperature will be certainly higher, the relative variation in pressure will be comparable with the results from the experimental infrastructure. In this way it will be possible to validate the model with real data. The current typical deep water BOP configuration in offshore gulf of Mexico has has a pressure transducer in the lower marine riser package (LMRP). The current standard sampling rate is set to 1 sample per minute, which will be too low to accurately determine the pressure variations associated with surge and swab. Though, the sensor is connected with fiber optic cables which makes it possible to install high accuracy pressure transducers. The standard sensor is rated at a pressure range from 0 to 20.000 psi seen in figure A.6. The placement of the sensor make it ideal for pressure response from the well as it is directly hydraulically connected with the well as seen in figure A.7.

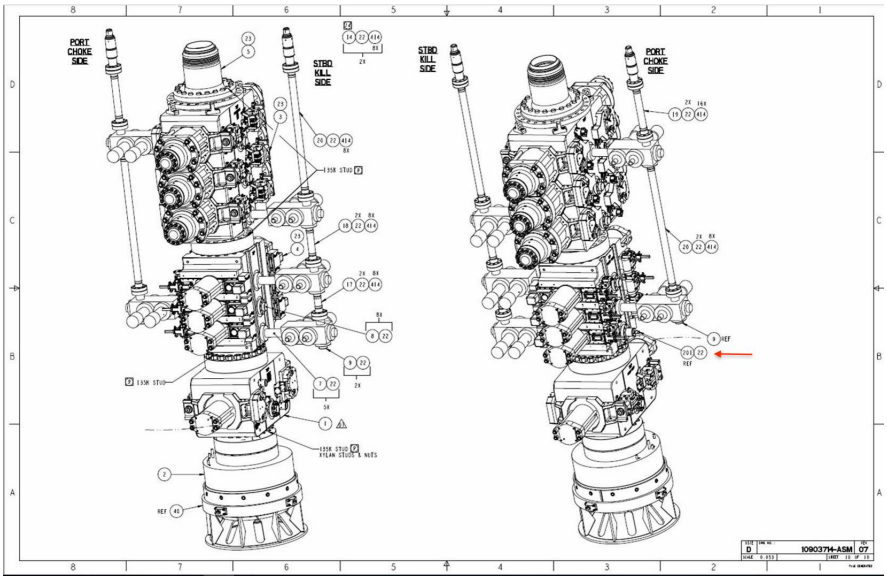

Figure 8.1: Typical deep water blow out preventer (BOP) configuration. Courtesy of Shell International Exploration and Production, 2020

On floating drilling vessels, the heave motion is continuously surveyed. Standard measuring points include block height with heave, heave height and heave velocity. These measurements are sampled every second with high precision. An example of this is seen in figure 8.2. Over a three hour time period, there are over 8000 heave data samples which allows for high accuracy in recreating the field conditions in the lab. Using this data together with pressure data from the HPHT sensor and a sample of the mud in use during the operation, it is possible to recreate the conditions to a high accuracy in the experimental infrastructure. Though the example shows a relatively low heave motion height. This is due to the drilling vessel being situated in the Gulf of Mexico, just outside the coast of Louisiana. In these waters, heave motion rarely exceed 1.00 m. Conditions in the North Sea will certainly show a larger heave motion and is an area of interest in regards to heave induced surge and swab.

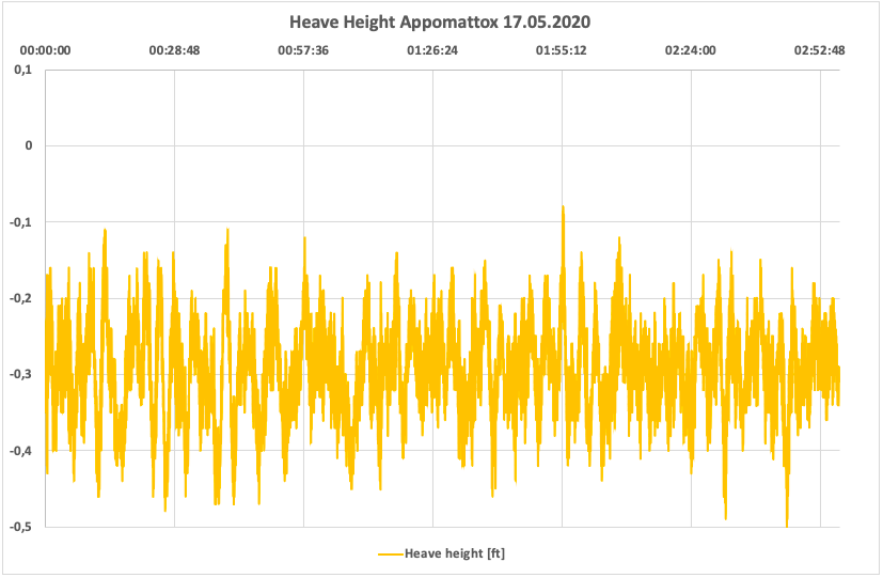

Figure 8.2: Sample of heave data from the floating drilling vessel Appomattox in the Gulf of Mexico on May 17th. Courtesy of Shell International Exploration and Production, 2020

Chapter 9

Conclusion

The ultimate ambition of the experimental infrastructure is to be field scalable and able to benchmark surge and swab models. With its functionality and promising initial results, the experimental infrastructure is a flagship within surge and swab quantification. With the scale and mode of action it is presumed to be field scalable. There is currently no other setup dedicated to the quantification of the drillstring dynamics and fluid mechanics associated with surge and swab.

The accuracy of sensors and reciprocating axial excitation from the linear motor will allow for a plethora of experimental opportunities. With the one metre stroke length compared to the length of the drillstring, it can simulate a variety of different scenarios encountered during drilling operations. The pressure transducers will give an accurate depiction of the pressure profile in the entire well during string movement. The positional sensors will additionally provide the necessary positional data to quantify the string excitation causing the pressure variation. With the constructed flowloop it is possible to exchange the test fluid in the well with relative ease which will allow for testing of a variety of drilling fluids. The supporting structure is designed to easily be dismantled for interchanging the drillstring to test with different string dimensions as well as being highly robust to endure substantial testing.

The way forward should entail an extensive testing of the experimental infrastructure. When its functionality and accuracy has been confirmed as well as optimization of the data processing program, experiments with water can be conducted. When the initial delay has been accounted for the lumped element model can be optimized. Once this model is is place, testing of fluids with rheologic parameters can be initiated. From the preceding rheologic study, the proposed drilling fluid representative consists of a water based glycerol solution. This will allow for an incremental approach to quantifying the non-Newtonian behaviour of drilling fluids, as glycerine only incorporate viscosity and exhibit Newtonian behaviour. When a compatible model has been created, field data can be tested. Through these experiments it will able to assess the scalability of the experimental infrastructure.

Bibliography

Anton Paar, G., 2010. Anton paar gmbh: e-learning course – basics of rheometry, part 1: Rotation; part 2: Oscillation. graz. URL: https://wiki.anton-paar.com/en/basics-of-rheology/#oscilliation-tests-and-viscoelasticity.

Anton Paar, G., 2020. Time-dependent behavior (oscillation). URL: https://wiki.anton-paar.com/en/time-dependent-behavior-oscillation/.

Arvani, F., Rideout, D., Butt, S., 2015. Dynamic model of a mobile offshore drilling unit in deep water environments for drilling simulation. ASME 2015 34th International Conference on Ocean, vol. 10, Offshore and Arctic Engineering, St. John, Canada. pp. 1–7 .

Bui, B., Saasen, A., Maxey, J., Ozbayoglu, M.E., Miska, S.Z., Yu, M., Takach, N.E., 2012. Viscoelastic properties of oil-based drilling fluids. Annual Transactions of the Nordic Rheology Society, Vol 20 .

Calkins, F.T., Fltau, A.B., Dapino, M.J., 2007. Overview of magnetostrictive sensor technology. Journal of Intelligent Material Systems and Structures 18; .

Cengel, Y.A., Cimbala, J.M., 2010. Fluid Mechanics: Fundamentals and Applications. McGraw Hill.

Crespo, F., Ahmed, R., 2012. A simplified surge and swab pressure model for yield power law fluids. Journal of Petroleum Science and Engineering 10 .

Crespo, F., Ahmed, R., Enfis, M., Saasen, A., Amani, M., 2012. Surge-and-swab pressure predictions for yield-power-law drilling fluids. SPE Drilling and Completion volume 27 .

Dhollm, 2017. Viscous regimes chart. URL: https://commons.wikimedia.org/wiki/File:Viscous_regimes_chart.png.

DIN, D.I.F.N., 2012. Modern rheological test methods - part 2: Thixotropy - determination of the time-dependent structural change - fundamentals and interlaboratory test. DIN SPEC 91143-2 .

Fontenot, J.E., Clark, R., 1974. An improved method for calculating swab and surge pressures and circulating pressures in a drilling well. Society of Petroleum Engineers Journal 14 .

Gjerstad, K., Time, R.W., Bjorkevoll, K.S., 2013. A medium-order flow model for dynamic pressure surges in tripping operations. Society of Petroleum Engineers Journal .

Gloassary, S.O., 2017. Rheological models. URL: https://www.glossary.oilfield.slb.com/en/Terms/r/rheology.aspx.

Hovda, S., 2018. Semi-analytical model of the axial movements of an oil-well drillstring in vertical wellbores. Journal of Sound and Vibration .

Huang, L., Zhang, Y., Zhang, L., Liu, M., 2008. Thixotropy in water-based drilling fluids. Annual Transactions of the Nordic Rheology Society, Vol 16 .

IADC, 2015. IADC Drilling Manual, 12th edition. International Association of Drilling Contractors (IADC) 200+ Authors, Houston, Texas.

Khalil, M.F., Kassab, S.Z., Adam, I.G., Samaha, M., 2008. Laminar flow in concentric annulus with a moving core. Twelfth International Water Technology Conference, IWTC12 2008 Alexandria, Egypt .

Landet, I., Parlov, A., Aamo, O., 2013. Modeling and control of heave-induced pressure fluctuations in managed pressure drilling. IEEE Transactions on Control Systems Technology 21 (4), 1340–1351 .

LinMot, 2020. Linear motors p10-70x320u. URL: https://shop.linmot.com/E/ag1000.70.320/linear-motors/linear-motors-p10-70/stators-ps10-70x320/ps10-70x320u-bl-qj-d01.htm.

Mabrouk, R., Guy, C.C., 2006. Effective drag coefficient investigation in the acceleration zone of an upward gas–solid flow. Chemical Engineering Science 62 .

Maxey, J., 2007. Thixotropy and yield stress behavior in drilling fluids. AADE-07-NTCE-37 .

Moore, P.L., 1974. Drilling practices manual, chapter 9 surge and swab pressures. Society of Petroleum Engineers .

Nazari, T., Hareland, G., Azar, J., 2010. Review of cuttings transport in directional well drilling: Systematic approach. SPE Western Regional Meeting held in Anaheim, California. SPE 132372 .

Olivieri, S., Picano, F., Sardina, G., Iudicone, D., Brandt, L., 2014. The effect of the basset history force on particle clustering in homogeneous and isotropic turbulence. Physics of Fluids (1994-present) 26, 041704 (2014); doi: 10.1063/1.4871480 .

Pannala, S., Syamlal, M., O'Brien, T.J., 2011. Computational Gas-Solids Flows and Reacting Systems: Theory, Methods and Practice. Engineering Science Reference (an imprint of IGI Global).

Pumpen, W., 2020. Progressing cavity pumps kb-s/kl-s. URL: https://www.wangen.com/pdf/en/Produktprospekt_KB-S_KL-S_EN_web.pdf?m=1587994436&.

Ramsey, M.S., 2019. Practical Wllbore Hydraulics and Hole Cleaning. Unlock Faster, More Efficient, and Trouble-Free Drilling Operations. Elsevier.

Regjeringen, 2020. Nasjonale tiltak [online accessed june 16 2020]. URL: https://www.regjeringen.no/no/tema/Koronasituasjonen/nasjonale-tiltak/id2693684/.

Sandahl, B., Sørgård, C., 2019. Tpg4565 rheology report. TPG Fordypningsemne.

Sarker, M., Rideout, D., Butt, S., 2012. Dynamic model of an oilwell drillstring with stick-slip and bit-bounce interaction. Proc. International Conference on Bond Graph Modeling, Genoa, Italy .

Sarpkaya, T., 2010. Wave Forces on Offshore Structures. Cambridge University Press.

Skalle, P., 2011. Drilling Fluid Engineering. Ventus Publishing ApS.

Sørgård, C., 2019. Design of experimental setup for describing surge and swab effects in typical drilling environments. TPG4560 Specialization Project.

Tehrani, A., 2007. Behaviour of suspensions and emulsions in drilling fluids. Annual Transaction of the Nordic Rheology Society, Vol 15 .

Tehrani, A., 2008. Thixotropy in water-based drilling fluids. Annual Transactions of the Nordic Rheology Society, Vol 16 .

Tobro, H.L., 2018. Review of a Semi-Analytical Drillstring Model Through Experimental Testing of Axial Motion. Master's thesis. NTNU - Norwegian University of Science and Technology.

Tucker, R., Wang, C., 1999. An integrated model for drill-string dynamics. Journal of Sound and Vibrations 224 123-165 .

Tucker, R., Wang, C., 2000. A simple cosserat model for the dynamics of drill-strings. The Seventh International Congress on Sound and Vibration, ICSV. .

Tveit, A., 2016. Prediction of Surge and Swab from Field Data Compared with Existing Theory. Master's thesis. NTNU - Norwegian University of Science and Technology.

White, F.M., 2010. Fluid Mechanics, Seventh Edition. McGraw Hill.

Zhang, Y., Liu, W., Zhang, H., Yang, J., Zhao, H., 2011. Design and analysis of a differential waveguide structure to improve magnetostrictive linear position sensors. MDPI Sensors Volume 11 Issue 5 .

Zhao, D., Hovda, S., Sangesland, S., 2016. Abnormal down hole pressure variation by axial stick-slip of drillstring. Journal of Petroleum Science and Engineering 145, 194-204 .

Appendix

Appendix A

Supporting Documents

Date	Lab Hours [h]	Note Work
06/05/2020	8,0	Dismantling of exsisting setup.
03/06/2020	4,5	Assembly of new experimental setup with new sensors. Casing, sensors, wires and flow tube.
04/06/2020	4,0	Waiting on equipment and welding
05/06/2020	8,0	Installing Drillpipe (10 full sections, 1 x 1.8m . To offset the thread connections between casing and DS). Hung off in slips.
08/06/2020	7,0	Installing ground foundation. Had to move due to alignment with counterweight guide installment. New fittings to the floor. Counterweight cut and threaded.
09/06/2020	6,0	Adjustment of the foundation of the setup. Cutting grooves into the pilars to allow for adjusting. Welding top mount of the counterweight guide and securing it.
10/06/2020	5,0	Machine work. Installed guide and connection for DS and adjusted height in well.
11/06/2020	6,0	Machine work. Counterweight groove and guide buchings were made. Chain mount and lifting bracket constructed. Ready for assembly
12/06/2020	0,0	Waiting on parts
13/06/2020	0,0	Weekend
14/06/2020	0,0	Weekend
15/06/2020	7,0	Mounted counterweight, motor, flywheel, chain and actuators (axial). Full weight is not supported by counterweight, need to ad 27 kgs to it.
16/06/2020	7,0	Mounted new counterweight. Shortened chain. Plexiglass protectors mounted as the magnet slider will stick to frame. Motor unit tested = works.
17/06/2020	7,0	Made cable canal and fixed wires. Started to wire sensory cables and feed cable. Waiting on parts to complete.
Sum	**69,5**	

Figure A.1: Lab hours constructing the experimental infrastructure.

Technical Data P10-70x320U/1130				
Stroke				
Max. Stroke	mm	(in)	1130	(44.49)
Force				
Max. Force[1] @ 1x230VAC	N	(lbf)	2170	(487)
Max. Force[1] @ 3x400VAC	N	(lbf)	2180	(489)
Max. Cont. Force [Passive cooling/ Fan / Fluid]	N	(lbf)	260 / 400 / 700	(58 / 89 / 160)
Max. Border Force relative	%		100	
Force Constant 1	N/A_{pk}	(lbf/A_{pk})	64	(14.4)
Force Constant 2	N/A_{rms}	(lbf/A_{rms})	90.5	(20.3)
Velocity				
Max. Velocity @ 1x230VAC	m/s	(in/s)	2.8	(109.9)
Max. Velocity @ 3x400VAC	m/s	(in/s)	4.9	(4.9)
Position Detection				
Repeatability	mm	(in)	±0.05	(±0.002)
Linearity	%		± 0.15	
Electrical Data				
Max. Current[1] @ 1x230VAC	A_{pk} / A_{rms}		33.7 / 23.8	
Max. Current[1] @ 3x400VAC	A_{pk} / A_{rms}		33.9 / 23.9	
Max. Cont. Current 1 [Passive cooling /Fan / Fluid]	A_{pk}		4.1 / 6.2 / 11	
Max. Cont. Current 2 [Passive cooling /Fan / Fluid]	A_{rms}		2.9 / 4.4 / 7.7	
Thermal Data				
Max. Winding Temperature (Sensor)	°C		90	
Thermal Resistance [Passive cooling / Fan / Fluid]	°K/W		0.65 / 0.28 / 0.09	
Thermal Time Constant [Passive cooling / Fan / Fluid]	s		2100 / 500 / 110	
Mechanical Data				
Slider Length	mm	(in)	1590	(63)
Slider Mass	g	(lb)	7470	(16.43)

1) Real time calculation of motor winding temperature is required (including monitoring).
If temperature monitoring is only based on temperature sensor signal (missing thermal model calculation), 60 % of the peak value has to be taken instead.

Figure A.2: Technical data for the LinMot P10-70x320U/1130 motor.

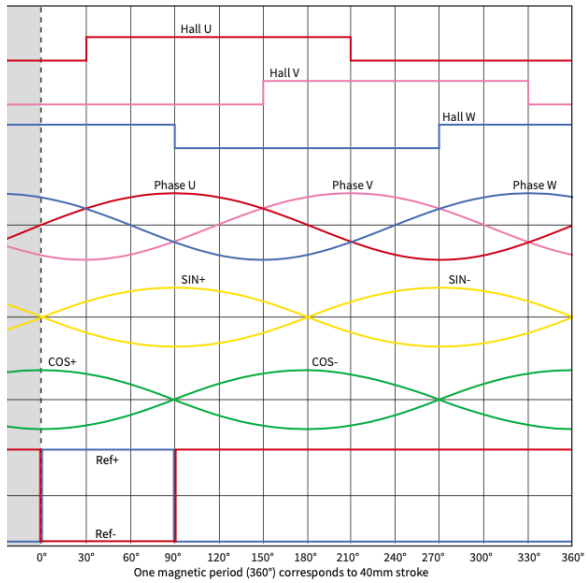

Figure A.3: Relationship between the phase current and the position sensor output in the P10-70x320U Motor. SIN+ and SIN- Encoder Signals are Always in Phase With Motor Current Phase U

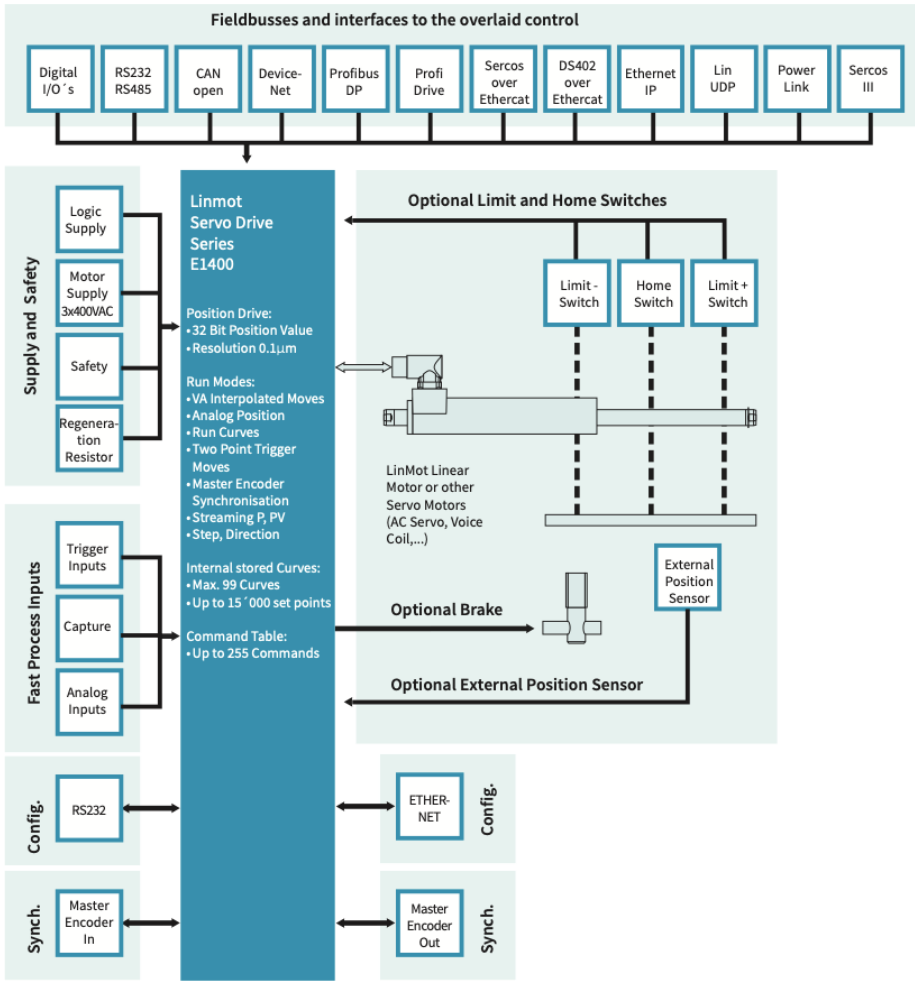

Figure A.4: Technical data for the LinMot E1400 servo drive

Design alteration appraisal

06.02.2020 Christoffer Sørgård

In further work with the surge and swab experimental setup it is desirable to improve both the agitation force, pressure sensors and experimental well fluid. This is to have more industry representative experiments and a wider range of experiment options. These implementations are desirable in further work both with the participation of a third-party company and without. The proposed drilling mud additives are Glycerol and Xanthan gum. An estimate of the volumes required, and bulk price is presented.
The investment will be a linear driving force motor and a titanium submersible pressure transmitter as well as the mud additive. The cost and specifications are outlined in the tables below.

Linear Motor Proposal and Appraisal

Article No	Article	Price [NOK]
0150-1284	PS10-70x320U-BL-QJ (Stator)	16 412,-
0150-2206	PL10-28x1590/1540 (Slider)	22 397,-
0150-1779	E1400-GP-QN-0S (Servo drive)	14 751,-
0150-2266	KPS15-04-L/Q-3 (Motor cable, 3m)	1553,-
0150-2263	KSS05-02/08-D15/J-3 (Encoder cable, 3m)	1377,-
		56 490,-

Pressure Transmitter Proposal

Article No	Article	Price [NOK]
107301	Druck PTX57N2, 0-5barg, 71m kabel. Trykktransmitter PTX57N2-TA-A2-CA-H0-PW	23 904,- 5 976,- (MVA)
		29 880,-

Experimental Well Fluid Options

Additive	Amount	Bulk Price	Total price
Glycerol	166,35 [L]	170,- [NOK/L]	28 280,-
Xanthan Gum	2,62 [Kg]	3000,- [NOK/Kg]	7 860,-
*Amounts are based on a total system volume of 262 Litres. With the introduction of a possible mixing tank, this number will increase.			

Summary

Investment	Price [NOK]
Linear Motor	56 490,-
Pressure Transmitter	29 880,-
Well fluid	
- Glycerol	28 280,-
- Xanthan Gum	7 860,-
Sum	
- **Glycerol**	**114 650,-**
- **Xanthan Gum**	**94 230,-**

Figure A.5: Design alteration appraisal submitted by 6th of February and approved by the institute the 12th of February

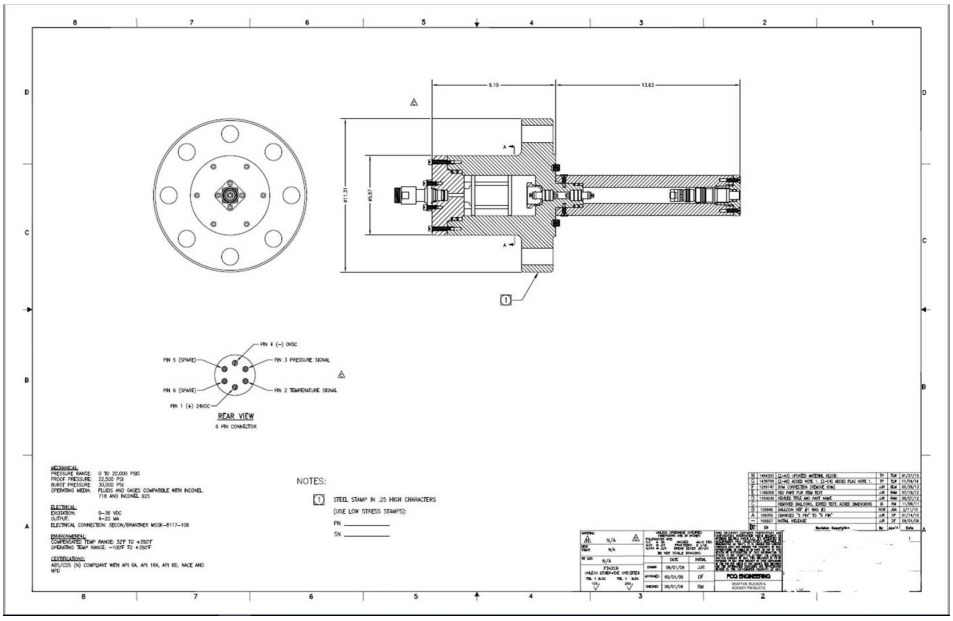

Figure A.6: Standard lower marine riser package HPHT sensor mounted to the BOP stack. Pressure rated from 0 to 20.000 Psi. Courtesy of Shell International Exploration and Production, 2020

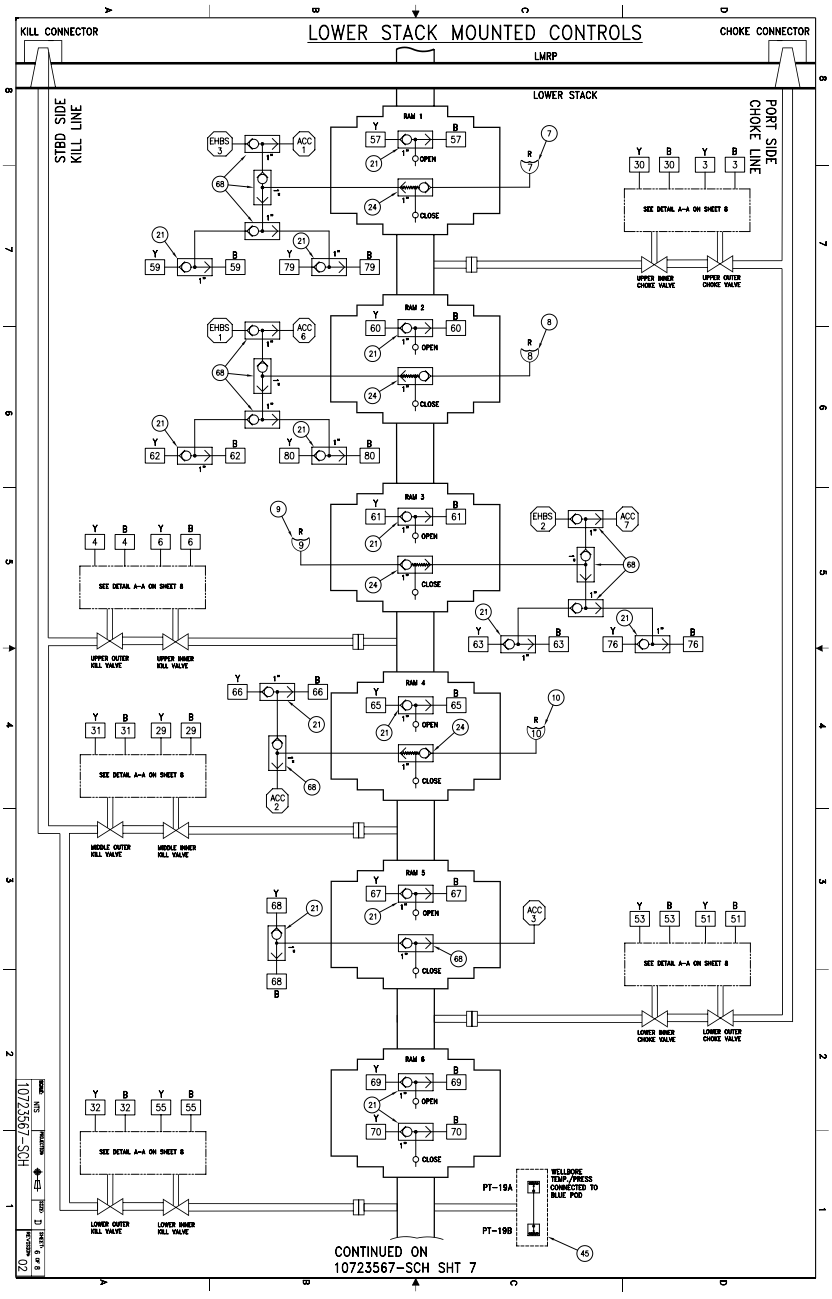

Figure A.7: Lower marine riser package with HPHT sensor indicated by (45) below Ram 6 at the lower right in the figure. Courtesy of Shell International Exploration and Production, 2020

Appendix B

Experimental Infrastructure

Figure B.1: Safety board instructing required personal protective equipment (PPE) during construction of the experimental infrastructure. From left: Eye protection, Breathing mask, protective footwear, hard hat and hearing protection above.

Figure B.2: Casing Mounted in Slips with PVC Sleeve for Temperature Sensor Mount and Steel Spacer below to Avoid Any Damage to the Sensor Fitting

Figure B.3: Casing bottom with magnetostrictive, temperature and pressure sensors. Flow loop valve with control tubes

Figure B.4: T-joint pressure sensor mount between casing sections. Here during disassembly with water pushed out by the hydrostatic column of remaining water within the casing above the T-joint

Figure B.5: Surface slips and casingstring mounted to steel garters at surface

Figure B.6: Brass end piece representing the bit and acting as a funnel guide for the magnetostrictive sensor rod at casing bottom

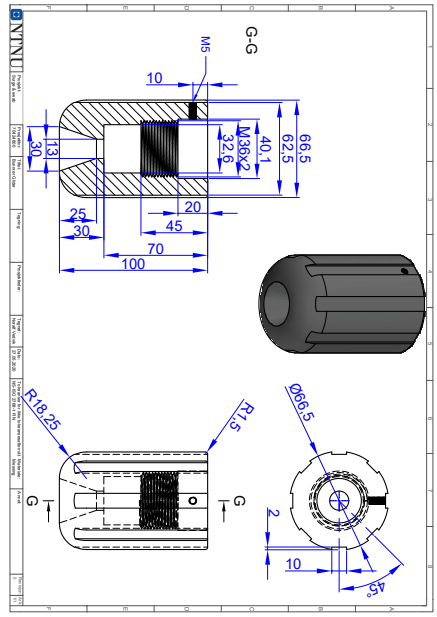

Figure B.7: Brass end piece representing the bit and acting as a funnel guide For the magnetostrictive sensor rod at casing bottom schematic. Courtesy of Vedvik, 2020

Figure B.8: Rounded crossover between BHA and drillpipe

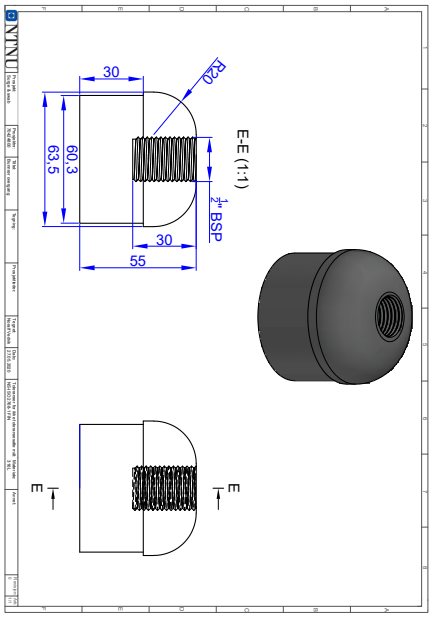

Figure B.9: Rounded crossover between BHA and drillpipe schematic. Courtesy of Vedvik, 2020

Figure B.10: Drillstring mounted in surface slips after assembly with sensory cables and flow loop hose running paralell.

Figure B.11: Drillstring counterweight and supporting structure before assembly.

Figure B.12: Counterweight with plastic guides for sliding within the supporting structure. Counterweight and guide grooved out to account for a weld within the supporting structure.

Figure B.13: Mounting of supporting structure for counterweight and motor assembly. Making grooves in the bottom foundation in order to have adjustment possibilities of the structure. Completed in order to properly center the linear motor above the drillstring.

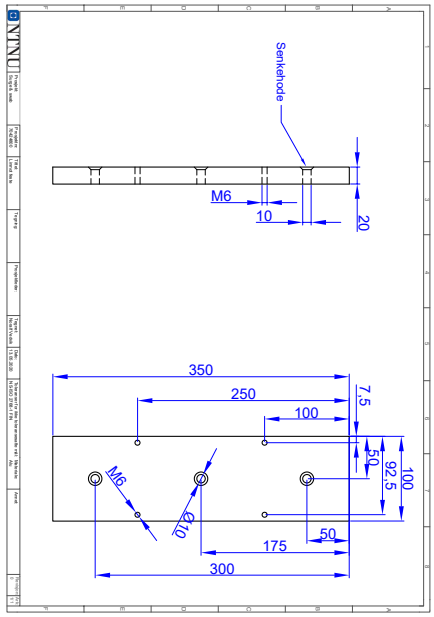

Figure B.14: Mounting plate for linear motor on supporting structure. Courtesy of Vedvik, 2020

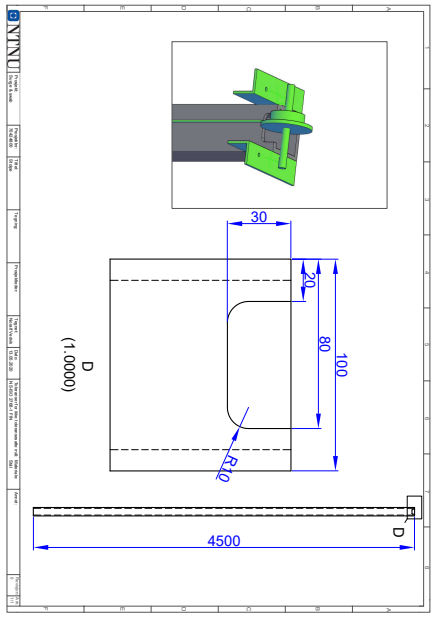

Figure B.15: Chain sprocket at top of supporting structure. Courtesy of Vedvik, 2020

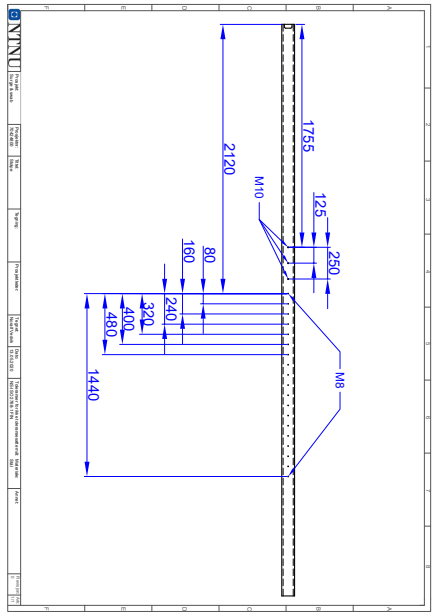

Figure B.16: Guide rail for guide block to which the linear motor and drillstring is attached. Courtesy of Vedvik, 2020

Figure B.17: Supporting structure mounted with guide rail and drillstring attached to slide block

Figure B.18: Slide block mounted to guide rail and drillstring with mount for linear motor

Figure B.19: Linear motor attached to supporting structure attached to sliding block

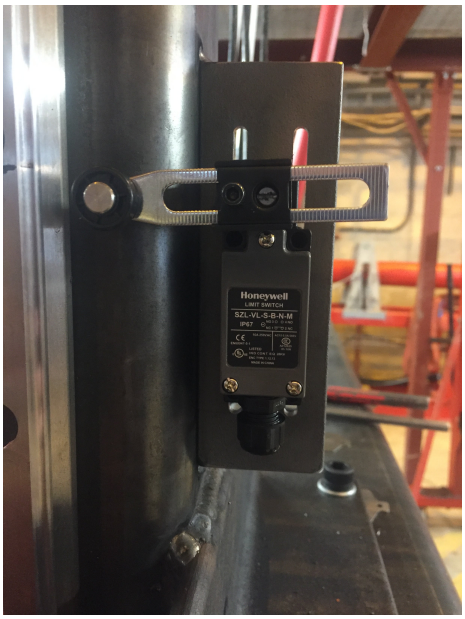

Figure B.20: Honeywell SZL-VL-S-B-N-M Miniature industrial limit switch

Figure B.21: Motor and sensory cables attached to the cable canal running into the junction box.

Figure B.22: Steel cogwheel with bearings for chain connecting linear motor and counterweight

Appendix C

Flow Curves from Rheologic Classification

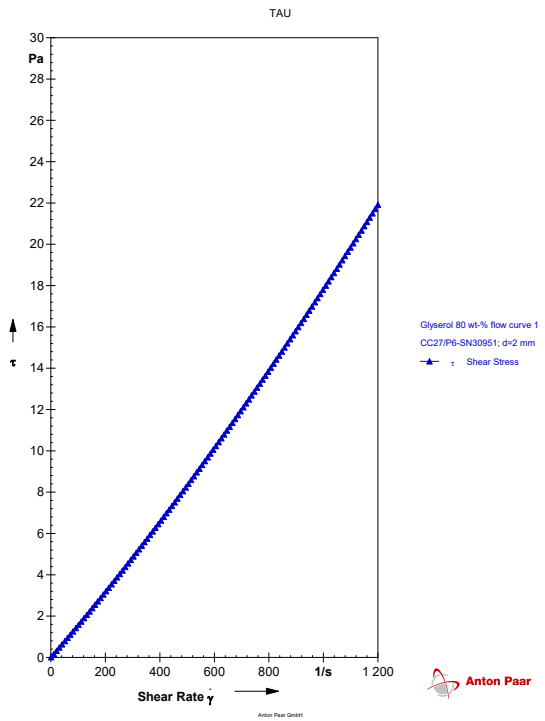

Figure C.1: Anton-Paar MCR 302 Flow curve test with 80 wt-% Glycerol solution. Expressing Newtonian behaviour as it coincides with Newtons law of viscosity ,stated in equation 3.9, with a linear relationship between shear stress,τ, and shear rate,$\dot{\gamma}$.

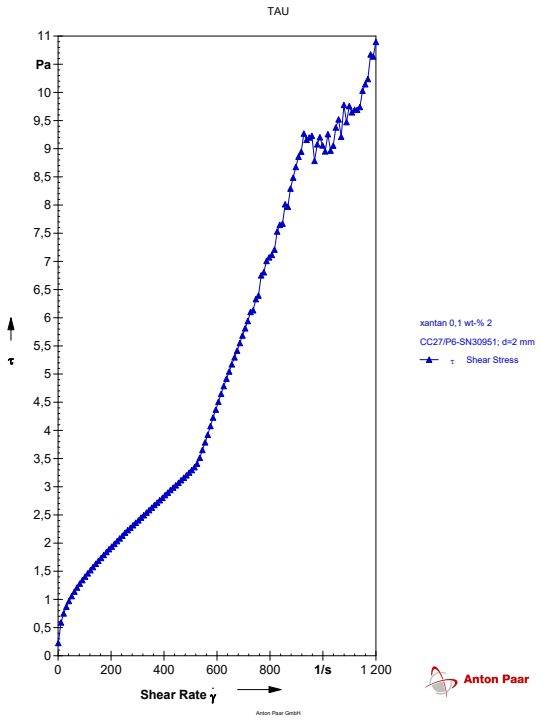

Figure C.2: Anton-Paar MCR 302 Flow curve test with 0.1 wt-% Xanthan gum solution. Expressing non-Newtonian behaviour as it deviates from Newtons law of viscosity ,stated in equation 3.9, with a a non-linear relationship between shear stress,τ, and shear rate,$\dot{\gamma}$.

Appendix D

Results from Preliminary Experiments

Figure D.1: Step test 2 positional sensor data from linear motor and bottom hole magnetostrictive sensor rod. Data Acquisition malfunction when compiling to file. Last 25 seconds was logged but plot data did not process. Stroke length set to 100 millimetres.

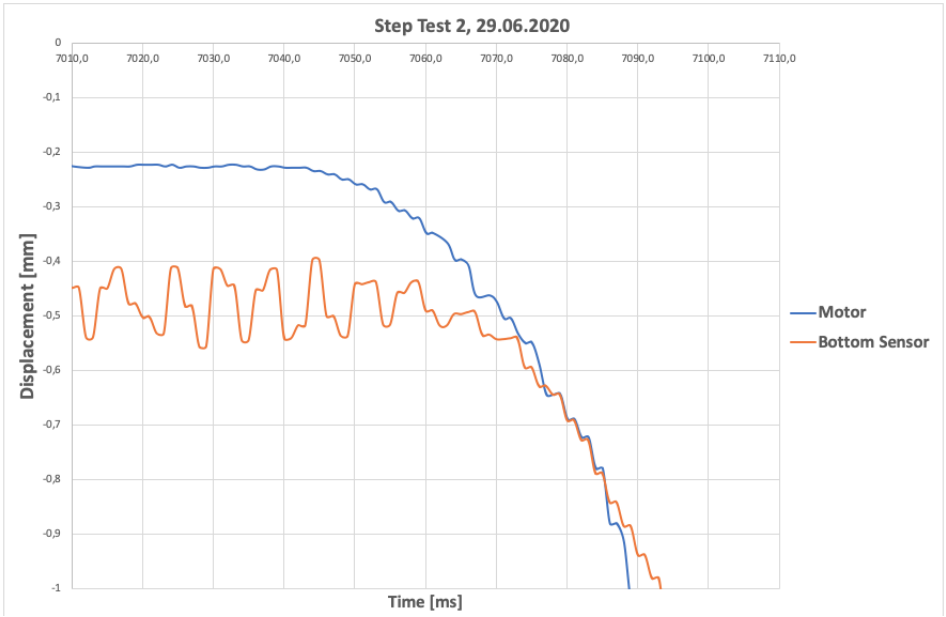

Figure D.2: Step test 2 of experimental infrastructure. A scaled plot of the difference in motor sensor positional data and bottom hole magnetostrictive sensor rod data. Delay equals approximately 25 milliseconds.

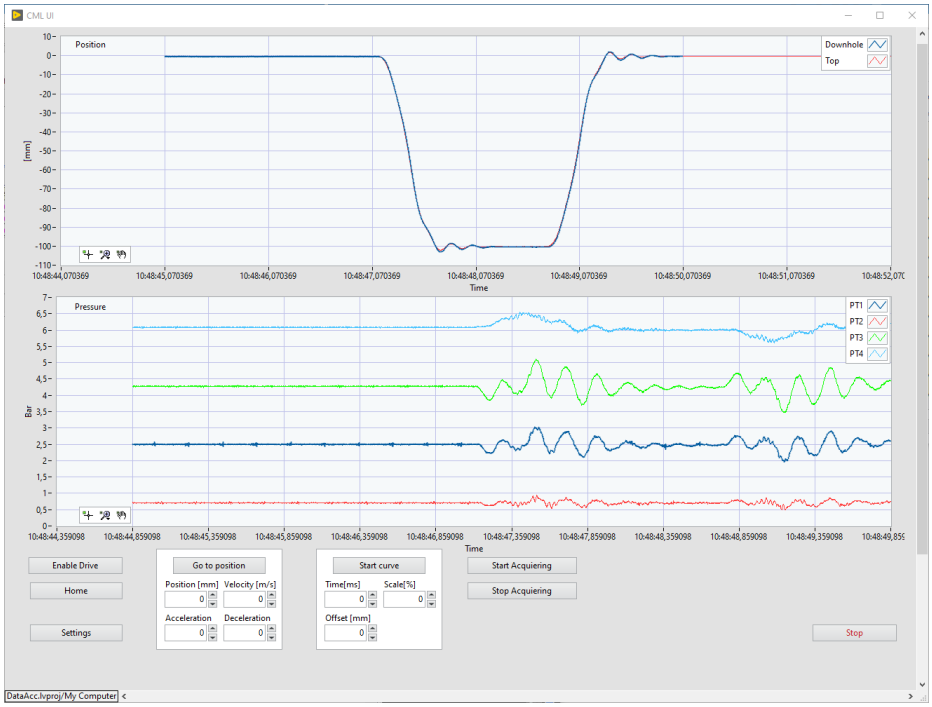

Figure D.3: Step test 2 raw data from the data acquisition program LabVIEW. Top plot indicating positional sensors. Bottom plot indicating pressure sensor response. Error in labeling, PT1 and PT2 legend is switched. Red line is PT1 and dark blue is PT2. Sensors responding to the movement of the drillstring. Measured surge and swab pressures equal approximately 0.5 bar.

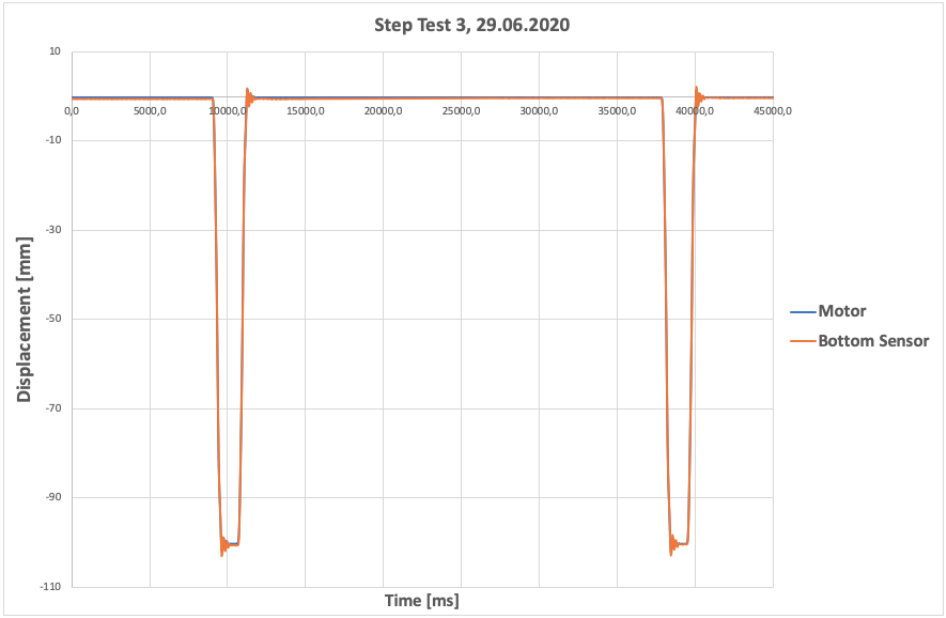

Figure D.4: Step test 3 positional sensor data from linear motor and bottom hole magnetostrictive sensor rod. Stroke length set to 100 millimeters. Total test time set to 45 seconds.

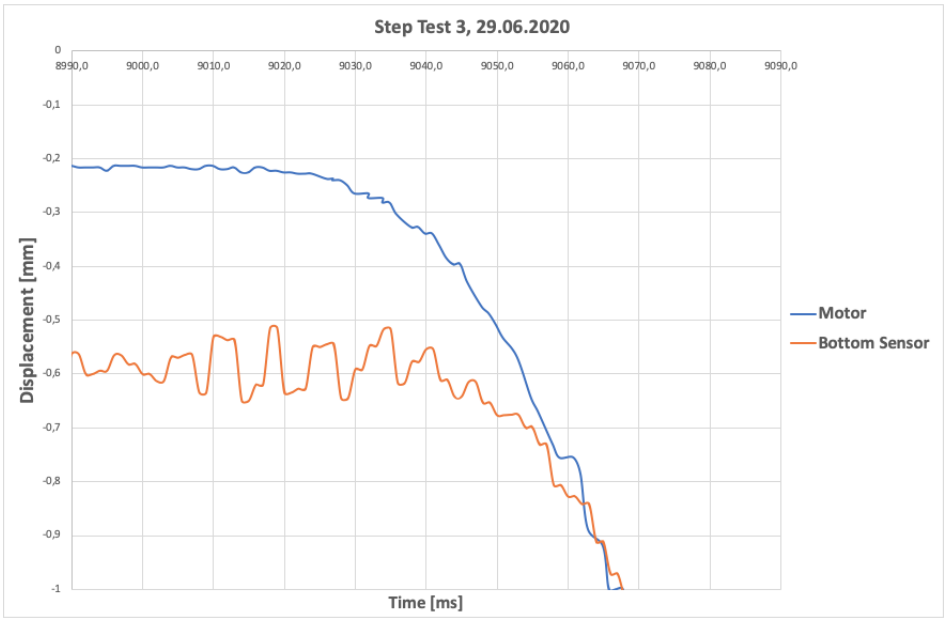

Figure D.5: Step test 3 of experimental infrastructure. A scaled plot of the difference in motor sensor positional data and bottom hole magnetostrictive sensor rod data. Delay equals approximately 30 milliseconds.

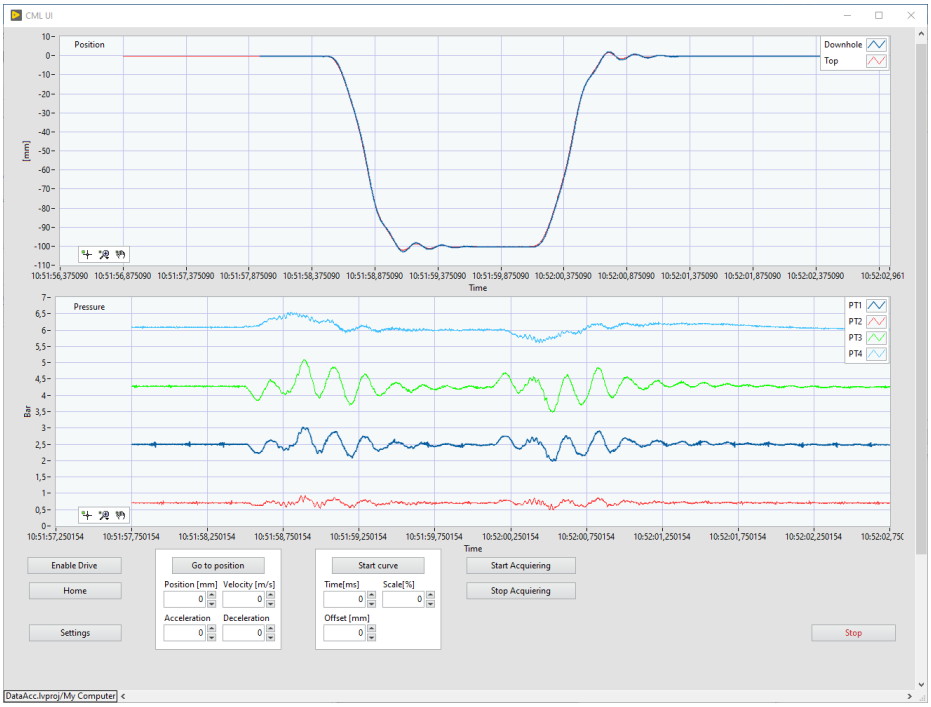

Figure D.6: Step test 3 raw data from the data acquisition program LabVIEW. Top plot indicating positional sensors. Bottom plot indicating pressure sensor response. Error in labeling, PT1 and PT2 legend is switched. Red line is PT1 and dark blue is PT2. Sensors responding to the movement of the drillstring. Measured surge and swab pressures equal approximately 0.5 bar.

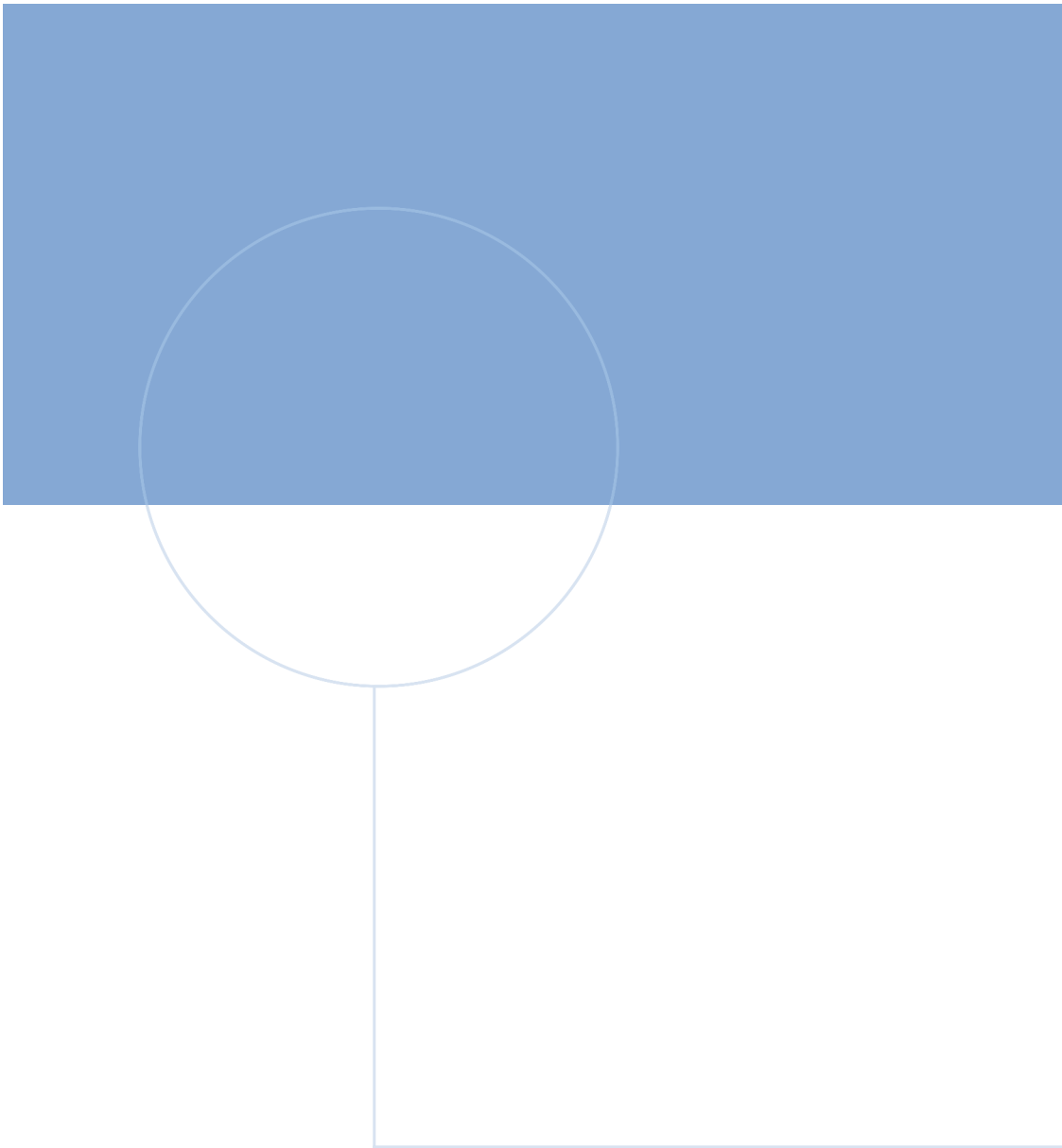

NTNU

Norwegian University of
Science and Technology